ADVANCED HEALTHCARE MATERIALS
www.advhealthmat.de

Spatiotemporal Regulation of the Bone Immune Microenvironment via Dam-Like Biphasic Bionic Periosteum for Bone Regeneration

Zonghan Xu, Liang Wu, Yu Tang, Kun Xi, Jincheng Tang, Yichang Xu, Jingzhi Xu, Jian Lu, Kaijin Guo,* Yong Gu,* and Liang Chen**

The bone immune microenvironment (BIM) regulates bone regeneration and affects the prognosis of fractures. However, there is currently no effective strategy that can precisely modulate macrophage polarization to improve BIM for bone regeneration. Herein, a hybridized biphasic bionic periosteum, inspired by the BIM and functional structure of the natural periosteum, is presented. The gel phase is composed of genipin-crosslinked carboxymethyl chitosan and collagen self-assembled hybrid hydrogels, which act as the "dam" to intercept IL-4 released during the initial burst from the bionic periosteum fiber phase, thus maintaining the moderate inflammatory response of M1 macrophages for mesenchymal stem cell recruitment and vascular sprouting at the acute fracture. With the degradation of the gel phase, released IL-4 cooperates with collagen to promote the polarization towards M2 macrophages, which reconfigure the local microenvironment by secreting PDGF-BB and BMP-2 to improve vascular maturation and osteogenesis twofold. In rat cranial defect models, the controlled regulation of the BIM is validated with the temporal transition of the inflammatory/anti-inflammatory process to achieve faster and better bone defect repair. This strategy provides a drug delivery system that constructs a coordinated BIM, so as to break through the predicament of the contradiction between immune response and bone tissue regeneration.

1. Introduction

In recent years, clinical treatments, including bone grafting, artificial bone, tissue-engineered bone, and bone handling techniques, have been established for bone defects caused by trauma, tumors, and bone diseases. However, 5%–10% of patients with fractures still suffer from bone nonunion or delayed union because the physiological function of the periosteum is underestimated.[1] The periosteum, a thin, tough, highly vascularized, connective tissue bilayer membrane covering the surface of bone tissue, acts as the "umbilical cord" of bone tissue by providing more than 70% of the blood supply and, furthermore, serves as a physical barrier that not only resists excessive infiltration of inflammatory cells but also creates a supportive microenvironment for bone marrow mesenchymal stem cells (BMSCs) to promote bone regeneration.[2] More importantly, severe soft tissue injury around a bone defect and the patient's underlying disease can cause disruption of the local immune microenvironment and secretion of excessive inflammatory factors, leading to tissue necrosis and bone nonunion.[3] In the past decade, various artificial periostea have been constructed to promote the repair of bone defects, such as macrostructural or microstructural bionic periosteum, vascularized bionic periosteum, and externally stimulated bionic periosteum.[2a,4] Although these bionic periostea promote bone regeneration in terms of structure and function, they are still less effective than the natural periosteum because the immune microenvironment around the fracture has been neglected in the design of artificial periostea. Therefore, in view of the role of the natural periosteum in physical blocking, immune regulation, osteogenesis, and angiogenic differentiation, preparing bionic periostea that can actively modulate the immune microenvironment is a reliable approach to enhance bone regeneration.

The bone immune microenvironment (BIM), composed of various immune cells and secreted cytokines, plays an important regulatory role in bone repair.[5] Macrophages (Mφ) are key mediators of the immune response and play a complex and sophisticated regulatory role in bone regeneration owing to their plasticity and heterogeneity.[6] The traditional view is that

Z. Xu, L. Wu, Y. Tang, K. Xi, J. Tang, Y. Xu, J. Xu, J. Lu, Y. Gu, L. Chen
Department of Orthopedics
the First Affiliated Hospital of Soochow University
Orthopedic Institute
Soochow University
188 Shizi Road, Suzhou, Jiangsu 215006, P. R. China
E-mail: lujian@suda.edu.cn; guyong1019@suda.edu.cn; chenliang7737@suda.edu.cn
K. Guo
Department of Orthopedics
the Affiliated Hospital of Xuzhou Medical University
99 Huaihai West Road, Xuzhou, Jiangsu 221000, P. R. China
E-mail: 100002013003@xzhmu.edu.cn
The ORCID identification number(s) for the author(s) of this article can be found under https://doi.org/10.1002/adhm.202201661

DOI: 10.1002/adhm.202201661

Mφ polarize to the M1 macrophage subtype under the induction of the local microenvironment and, furthermore, secrete inflammatory factors such as IL-1β, IL-6, TNF-α, and INOS to promote an inflammatory response and osteoclast differentiation in the early stage of fracture. However, it has been found that M1 macrophages can regulate bone regeneration by secreting vascular endothelial growth factor (VEGF) and oncostatin-M (OSM) and thus are essential in bone regeneration.[7] Activated by local anti-inflammatory factors in the mid-to-late phase of inflammation, M2 macrophages secrete anti-inflammatory factors such as arginase-1 (arg-1) and interleukin-10 (IL-10) to promote tissue repair as well as active factors such as platelet-derived growth factor-BB (PDGF-BB), matrix metalloprotein-9 (MMP9), and bone morphogenetic protein-2 (BMP-2) to promote osteogenesis and angiogenesis.[7b,8] M1 and M2 intertwine and regulate each other at the inflammation, angiogenesis, and osteogenesis stages of bone regeneration, but the prolonged presence of either subtype leads to different malignant outcomes.[9] Therefore, simple inhibitory intervention of the M1-related inflammatory response and early or maximal promotion of M2 polarization are not sufficient to yield the desired bone regeneration effect. Sequential regulation of M1/M2 polarization at the right stage is crucial for bone regeneration.[10] Typically, the amount of bone healing inflammatory cytokines begins to decline 3 d after the implantation of biomaterials and anti-inflammatory related immune cells appear thereafter (days 4–7), but the process of spontaneous conversion of macrophages from proinflammatory M1 to anti-inflammatory M2 is inhibited by the microenvironment.[6b,11] Therefore, the key is to design a bionic periosteum that can precisely regulate the BIM, that is, a moderate inflammatory microenvironment in the early stage and an anti-inflammatory microenvironment thereafter (3 d after biomaterial implantation) to promote the polarization of M2.[12] However, endowing the bionic periosteum with the ability to regulate macrophage subtype transformation in sequence is an urgent problem that remains unsolved.

Currently, there are numerous studies on developing biomaterials with immunomodulatory effects, focusing on the modulation of Mφ phenotypes through material properties such as surface structure, intrinsic composition, and porosity. However, material properties cannot accurately and sequentially modulate the inflammatory response of the host owing to the complex biological environment.[11] Therefore, loading the biomaterial with appropriate cytokines and modifying the material surface to achieve controlled release of loaded cytokines is a feasible strategy to endow the material with the ability to accurately modulate the inflammatory response of the host. Micro-sol (MS) electrospinning can be used to prepare poly-L-lactic acid (PLLA) micro-sol electrospun fibers with a core–shell structure, which have the properties of high drug loading capacity, strong mechanical stability, and high operability.[4a] IL-4 is mainly produced by activated T cells and plays an important role in immune regulation. After binding to IL-4 receptors α (IL-4Rα) on the surface of Mφ, IL-4 activates not only JAK to mediate STAT6 phosphorylation for M2 polarization but also the PI3K/AKT signaling pathway to induce T helper 2 (Th2) cell immune responses.[13] Therefore, IL-4 is an appropriate active factor for loading into bionic periostea. However, a micro-sol electrospun fiber is hydrophobic and has no cell recognition units on its surface, which is not conducive to cell adhesion and proliferation. The primary concern is that the concentration difference between the inside and outside of the fiber triggers early burst release, which disrupts sequential regulation of the immune response. On this basis, hybridizing the matrix with functional materials to achieve biphasic binding may be a feasible strategy to tackle these limitations.[14]

Hydrogels are often used in controlled drug delivery systems because of their adjustable physicochemical properties and biodegradability. Hydrogels with superior biocompatibility and hydrophilicity have been widely used to coat matrix materials to obtain highly controlled drug delivery systems.[15] Hydrogels derived from the periosteal matrix can promote angiogenesis and bone regeneration through immune regulation.[16] Composites of electrospun fiber membranes and hydrogels inherit the high mechanical strength and strong barrier effect of the natural periosteum as well as the good biocompatibility of the hydrogel.[17] Thus, we postulated that a dense hydrogel coating can be constructed and attached to the surface of micro-sol electrospun fibers as the gel phase to capture and store IL-4 in the early stage, thus achieving spatiotemporal regulation of the immune response.[18] Carboxymethyl chitosan (CMC), a water-soluble derivative of chitosan, contains functional amino and carboxyl groups and exhibits good biocompatibility, hydrophilicity, and biodegradability.[19] In addition, CMC can chelate calcium ions to promote osteogenic activity.[20] However, simple CMC hydrogels suffer from swelling in water and lacks the necessary organic components of bone tissue. Type I collagen (Col-I), a natural extracellular matrix-like polymer, is rich in the RGD sequence to promote cell adhesion and has mineralization ability, which can compensate for the low adhesion ability and lack of organic components of simple CMC hydrogels.[21] However, the degradation rate of Col-I is faster than that of CMC and the effect of controlled release of IL-4 may be reduced using Col-1 only as the surface coating. Moreover, Col-I itself can cooperate with IL-4 to promote M2 polarization.[22] The simple use of Col-I as a surface coating will disrupt the establishment of a moderate inflammatory microenvironment in the early stage of inflammation. Genipin (GP) is a natural cross-linker that can react with primary amino groups. GP contains heterocycles and has a high degree of intermolecular entanglement, and thus 3D networks crosslinked by GP are stable and compact.[23] Therefore, CMC, Col-1, and GP were used in combination to construct the gel phase of the bionic bone membrane.

In this study, inspired by the dynamic characteristics of the BIM as well as the functional structure of the natural periosteum, we encapsulated IL-4 in the core structure of electrospun fibers using the micro-sol electrospinning technique and crosslinked CMC and Col-I on electrospun fibers with GP to form a dense layer of carboxymethyl chitosan-collagen (CMC-Col) coating (**Scheme 1**A).[24] The fiber phase was used to load and protect IL-4 as well as to provide the main mechanical support for the bionic periosteum. The gel phase was used to intercept and store the sudden release of IL-4 from the fiber phase, thus maintaining the moderate inflammatory reaction at the early inflammatory stage. As the gel phase degraded during the inflammatory repair phase, IL-4 was released markedly to mediate the polarization of Mφ to the M2 subtype. Anti-inflammatory and bone-repair related cytokines were secreted to construct paracrine-transformed BIM. TGF-β1, BMP-2, PDGF-BB, and MMP-9 de-

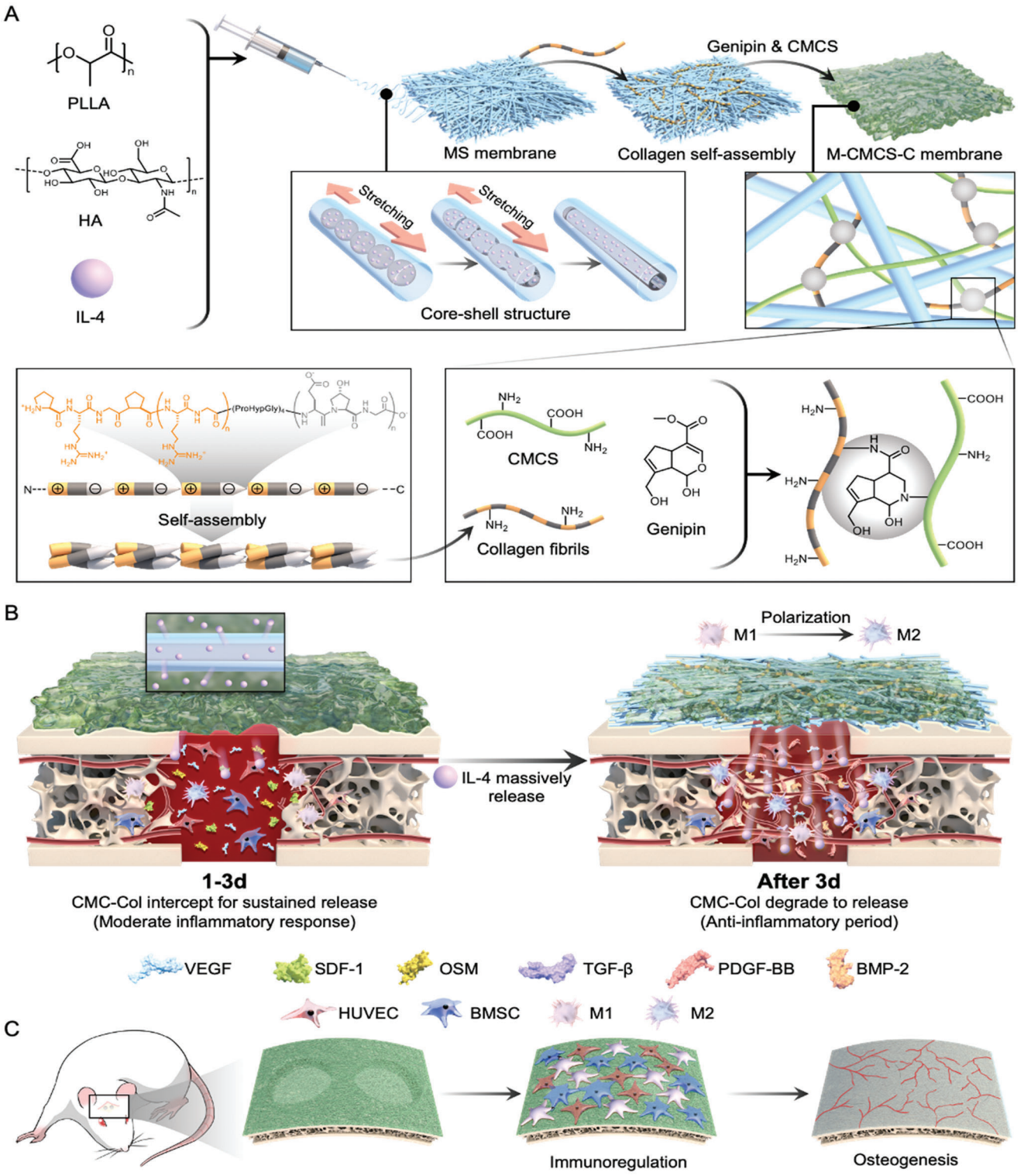

Scheme 1. Schematic illustration of the construction and application of biphasic bionic periosteum. A) Preparation of biphasic bionic periosteum (MS@CMC-Col) by coating carboxymethyl chitosan-collagen hydrogel (CMC-Col) on micro-sol electrospun fibers (MS). B) Controlled release of IL-4 maintains the moderate inflammatory microenvironment during the inflammatory period and promotes M2 polarization for an anti-inflammatory microenvironment after 3 d. C) Schematic diagram of the construction of the rat cranial defect models, implantation of the bionic periosteum, immune modulation, and bone regeneration.

rived from M2 cooperated with BMSCs and human umbilical vein endothelial cells (HUVECs) to promote local osteogenic and vascularization differentiation (Scheme 1B). Using a rat cranial defect model, we confirmed that the bionic periosteum coordinated the conversion of Mφ subtypes, thus achieving controllable conversion of the inflammatory microenvironment to an anti-inflammatory microenvironment, resulting in excellent bone defect repair (Scheme 1C).

2. Results and Discussion

2.1. Characterization of MS@CMC-Col

With the evolving concept of bone repair and the development of periosteal tissue engineering, researchers have prepared various structured and functional artificial periostea. However, there are few studies on the regulation of periosteal BIM, especially controlled regulation of the osteogenic microenvironment. In this study, micro-sol electrospinning technique was first used to prepare electrospun fibers with core-shell structure loaded with IL-4. Then MS@CMC-Col bionic periosteum was successfully prepared using the collagen self-assembly technique and natural cross-linker GP to apply a CMC-Col hydrogel coating on the MS surface (Figure S1, Supporting Information). Here, PLLA refers to PLLA electrospun fibers, MS refers to electrospun fibers prepared by micro-sol electrospinning, MS@Col refers to MS self-assembled with Col-I, PLLA@CMC refers to PLLA combined with CMC, and MS@CMC refers to MS combined with CMC. Scaffolds with MS in the name contain IL-4.

The surface morphologies of different electrospun fibers were observed using scanning electron microscopy (SEM) (**Figure 1**A). PLLA and MS were smooth and arranged randomly with high homogeneity. Analysis using ImageJ revealed that the average diameters of single fibers of PLLA and MS were respectively 057 $\pm$ 0.18 μm and 0.58 $\pm$ 0.17 μm, which were not statistically different from each other (Figure S2, Supporting Information). A dense and smooth hydrogel coating was observed on the surface of MS@CMC fibers. The SEM image of MS@Col, obtained after the collagen self-assembly with MS, (Figure S3, Supporting Information) showed that many collagen fibers were deposited on the electrospun fibers, forming a spiderweb-like structure. MS@CMC-Col, constructed by combining Col-I self-assembled fibers and CMC coating, was still covered with a dense hydrogel. However, compared with the CMC coating alone, the surface roughness of the CMC-Col coating increased owing to crosslinking between collagen fibers and CMC through GP, which was more suitable for cell adhesion.

The diameter of sodium hyaluronate (HA) micro-sol particles loaded with IL-4 was measured using dynamic light scattering (DLS) (Figure S4, Supporting Information). HA particles had an average size of 384.6 nm, with diameters ranging from 100 to 1000 nm and a polymer dispersity index (PDI) of 0.206, which indicated that the particle size was uniform. The prepared micro-sol particles did not change after they were left at room temperature for 2 h, suggesting a high stability of the particles for the encapsulation of IL-4.

An internal core–shell structure of MS is prerequisite for the high drug loading capacity of the bionic periosteum and the stable release of the loaded drug. The internal structure of the single fiber was observed using transmission electron microscopy (TEM) (Figure 1B). Compared with PLLA, there were distribution bands with a diameter of 0.16 $\pm$ 0.03 μm, which were formed by the stretching of HA particles inside MS, and the bands had a smooth surface and homogeneous structure. Fluorescently labeled bovine serum albumin (BSA) was used instead of IL-4 wrapped in HA particles for electrospinning with light avoidance. Labeled BSA was uniformly distributed inside each electrospun fiber (Figure 1C), which indicated stable drug loading by micro-sol electrospinning. The stability of micro-sol electrospun fibers is important for effective regulation of the osteogenic microenvironment by the bionic periosteum.

Energy dispersive X-ray spectroscopy (EDS) (Figure 1D) was used to clarify the changes in chemical composition on the surface of different electrospun fibers. Compared with the EDS spectra of PLLA and MS, which contained C and O, the EDS spectra of electrospun fibers with hydrogel coatings contained three elements: C, O, and N. Moreover, the N content in MS@CMC-Col increased to 13.53% because of the combination of Col-I self-assembly and CMC coating. Fourier transform infrared spectroscopy (FTIR) was used to analyze the molecular structures of different fibrous membranes (Figure 1E). The peak at 1750 cm^{-1} corresponded to the stretching vibration of C=O of PLLA. The infrared spectra of MS and PLLA were the same, with no characteristic HA peaks, which further confirmed that the micro-sol particles existed in the nuclear structure. Compared with MS, MS@Col showed characteristic peaks representing amide bonds at 3340 cm^{-1}, 1650 cm^{-1}, and 1550 cm^{-1}. After the integration of CMC and Col-I by GP, a new peak appeared at 1414 cm^{-1} due to the stretching vibration of GP, along with a stronger characteristic peak of the amide bond.[25] Overall, our findings confirmed that the gel phase of MS@CMC-Col was successfully constructed.

As biomaterials for implantation in the human body, good hydrophilicity can improve the biocompatibility and hemocompatibility of the material and facilitate cell adhesion, proliferation, and differentiation.[26] The water contact angles of PLLA, MS, PLLA@CMC, MS@CMC, and MS@CMC-Col were 122.3 $\pm$ 0.86°, 121.8 $\pm$ 1.67°, 40.45 $\pm$ 2.16°, 40.15 $\pm$ 1.27°, and 42.63 $\pm$ 2.20°, respectively (Figure 1F). The water contact angles of PLLA@CMC, MS@CMC, and MS@CMC-Col were significantly reduced, which indicated that the hydrophilicities of PLLA@CMC, MS@CMC, and MS@CMC-Col were greatly improved because of the gel phase. The improved hydrophilicity enhances the ability of the bionic periosteum to recruit and adhere cells.

In consideration of the strong forces exerted by the tissue surrounding bone defects, excellent mechanical stability is essential for the bionic periosteum. The mechanical properties of the bionic periosteum were investigated with mechanical tensile experiments, and the corresponding stress–strain curves were plotted. PLLA electrospun fibers had favorable mechanical properties (Figure 1G). Moreover, the mechanical strength of MS was lower than that of PLLA owing to the presence of the HA core. However, after the deposition of collagen fibers and crosslinking with CMC on the surface, the maximum tensile strength of MS@CMC-Col reached 5.01 $\pm$ 0.16 MPa, which was significantly greater than that of PLLA. Because many hydrogel molecules are bound within the pores of electrospun fibers, electrospun fibers

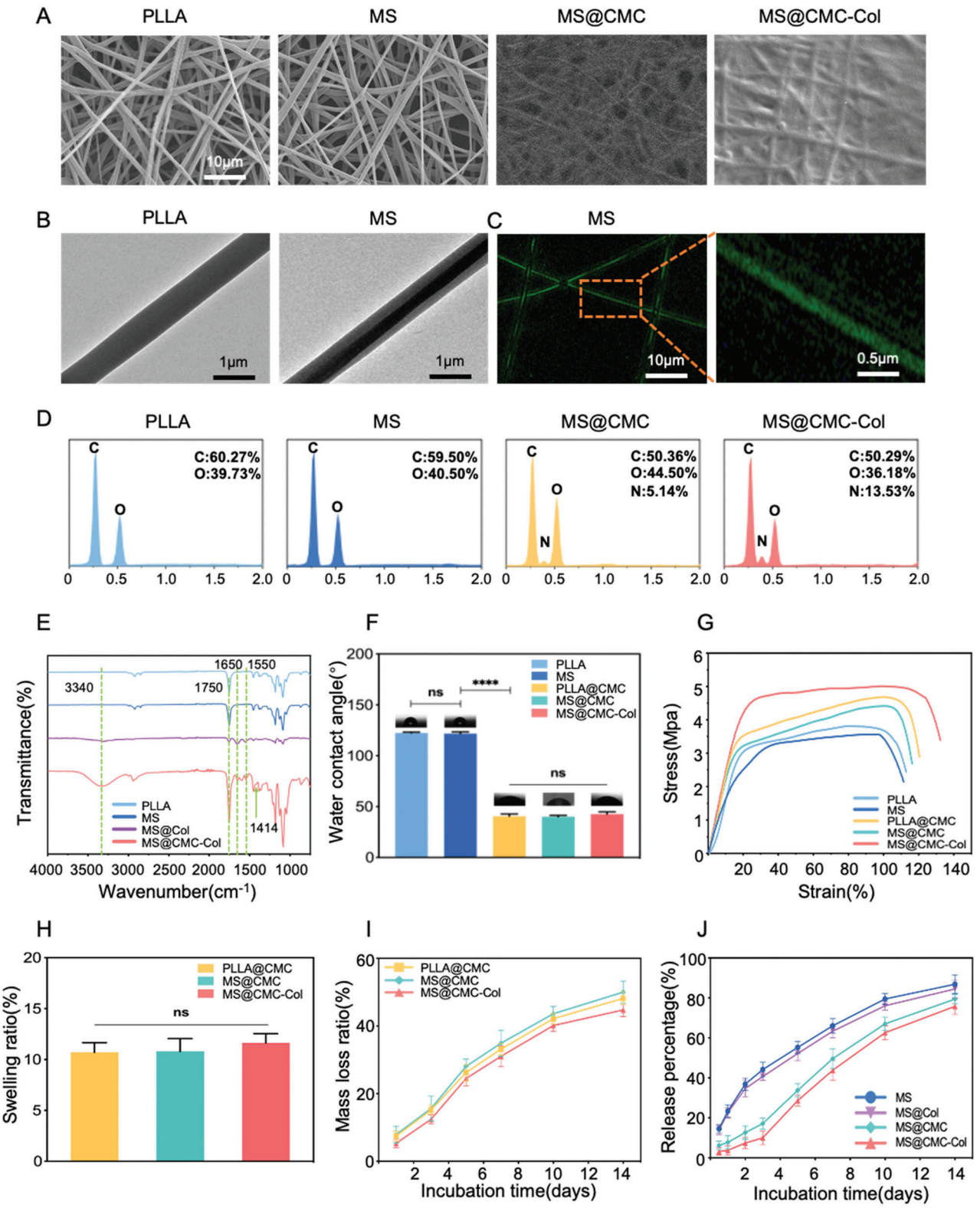

Figure 1. Morphology, chemical structure, and physicochemical properties of different electrospun fibers. A) SEM images. B) TEM images of PLLA and MS. C) Distribution of FITC-BSA in electrospun fibers. D) EDS elemental spectra. E) FTIR spectra of different electrospun fibers. F) Water contact angles of different electrospun fibers. G) Mechanical tensile testing of different electrospun fibers. H) Dissolution rate of different electrospun fibers. I) Degradation of different electrospun fibers. J) Release of IL-4 from different electrospun fibers in vitro. (Statistical analysis entails one-way ANOVA followed by Tukey's multiple comparison test; $n = 3$; ns, not statistically significant; ****$p < 0.0001$.)

with the hydrogel coating can counteract the effect of the core–shell structure and, furthermore, have significantly improved mechanical properties. Therefore, constructing a gel phase is important for improving the mechanical properties of the bionic periosteum.[27]

The swelling rate directly reflects the degree of crosslinking in the gel, that is, the higher the degree of crosslinking, the lower the swelling rate of the gel. The swelling rates of three different electrospun fibers with hydrogel coatings were lower than 15% (Figure 1H), indicating that the structure of the hydrogel coatings was complex and compact owing to the high degree of intermolecular entanglement of GP. The in vitro degradation experiment revealed that the degradation rates of three different electrospun fibers with hydrogel coatings were all lower than 20% in the first 3 d (Figure 1I), indicating that the 3D structure of the CMC and CMC-Col gel layers was dense and stable. A dense and stable structure of the gel phase is beneficial to control the sudden release of active factors (IL-4) in the fiber phase.

The in vitro release of the IL-4 in different electrospun fibers was investigated by enzyme-linked immunosorbent assay (ELISA) for IL-4 (Figure 1J). For MS and MS@Col, there was a significant, abrupt release during the first 3 d, in which 44.2 ± 3.7% and 40.6 ± 2.0% of IL-4 was released from inside the electrospun fibers, followed by a significantly decreased release rate. In contrast, for the hydrogel-coated biphasic gel-fiber, early abrupt release was suppressed owing to the dense gel coatings. The release of IL-4 from MS@CMC-Col was controlled to within 10% in the first 3 d, with increasing amounts of IL-4 released after 3 d. The amount of IL-4 released on day 14 reached 78.9 ± 2.58%. Due to the presence of heterocyclic rings and the high degree of intermolecular entanglement, GP can trigger a higher crosslinking degree, a more reticular structure, and a denser gel than the porous gel formed by physical crosslinking, thus intercepting the sudden release of IL-4. Additionally, CMC and collagen are rich in carboxyl and amino groups, which can adsorb IL-4 suddenly released from the fiber phase by covalent bonds to some extent. Overall, the gel phase can intercept and store the initial sudden release of IL-4 through its compact hydrogel network structure and the affinity adsorption to IL-4. The biphasic fiber membrane can change the early sudden release mode of IL-4 from microsol electrospinning and reduce the sudden release within 3 d but allowing the release of large quantities of IL-4 thereafter, thus realizing the spatiotemporal regulation.

2.2. In Vitro Experiments

2.2.1. Biocompatibility

Biocompatibility is an important theme in tissue engineering. In vitro experiments were used to evaluate the biocompatibilities of different electrospun fibers. BMSCs from bone tissue with multiphase differentiation potential were grown on different electrospun fibers for Live/Dead staining and CCK-8 assays. The Live/Dead staining results (Figure S5, Supporting Information) showed that the cells survived and proliferated on all groups of electrospun fibers, indicating that all electrospun fibers had no significant toxic or inhibitory effects on the cells. However, the number of live cells was significantly lower, and the number of dead cells was higher on PLLA than on hydrogel-coated electrospun fibers. MS@CMC-Col had more live cells than the other electrospun fibers and had no significant difference with the control group. This may be due to the presence of Col-I in the gel phase, which can mimic the extracellular matrix for cells. Similarly, in the CCK-8 essay (Figure S6, Supporting Information), BMSCs increasingly proliferated after 1, 3, 5, and 7 d of coculture with different electrospun fibers. From day 5 onwards, MS@CMC-Col had a significantly higher number of BMSCs than the other electrospun fibers and had no statistically difference with the control group. The good hydrophilicity, good adhesion, and low immunogenicity of MS@CMC-Col can greatly improve the biocompatibility of the material, which is a good basis for implantation of the bionic periosteum.

2.2.2. Cell Adhesion Promoted by Biphasic Bionic Periosteum

The mutual adhesion between seed cells and the biomaterial is the basis for the biological function of tissue engineering. Good adhesion on the biomaterial is essential for cell proliferation and differentiation. Integrin β1 is a family of cell adhesion molecules, and as a transmembrane protein receptor, it enables adhesion between cells and the extracellular matrix by forming focal adhesions (FAs), thus mediating signal transduction between the inside and outside of cells.[28] The fluorescence image of integrin β1 (**Figure 2**A) was semiquantitatively analyzed (Figure 2B), revealing that the red fluorescence was stronger in electrospun fibers with hydrogel coatings than in PLLA. Moreover, the fluorescence was stronger in MS@CMC-Col than in MS@CMC, which was attributed to the binding of integrin sites like RGD and GEFOGR with Col-I, thus enhancing the cell adhesion of the bionic periosteum.[29]

Vinculin is an important protein of FAs found at cell–cell or cell–extracellular matrix junctions. It mediates cell signaling by binding to cytoskeletal F-actin and plays an important role in cell adhesion, extension, proliferation, and differentiation.[30] The fluorescence image of vinculin (Figure 2C) was semiquantitatively analyzed (Figure 2D), revealing that vinculin anchored intracellular F-actin better in the three electrospun fibers with hydrogel coatings, among which MS@CMC-Col exhibited the strongest red fluorescence.

In summary, biphasic bionic periosteum coated with the CMC-Col hydrogel greatly improves the adhesion of the electrospun fibers, which allows it to mimic the extracellular matrix for cell adhesion and proliferation, providing a favorable platform for subsequent cell proliferation, differentiation, and biological functions.

2.2.3. Sequential Modulation of Mφ Polarization to Improve the Osteogenic Microenvironment

The local inflammatory response of bone defects is an important regulator of bone regeneration, and Mφ, as an important player in the inflammatory response, can be polarized in different immune microenvironments into the inflammatory subtype M1 or the anti-inflammatory subtype M2. M1 preferentially expresses CD86, while M2 preferentially expresses CD206. M1

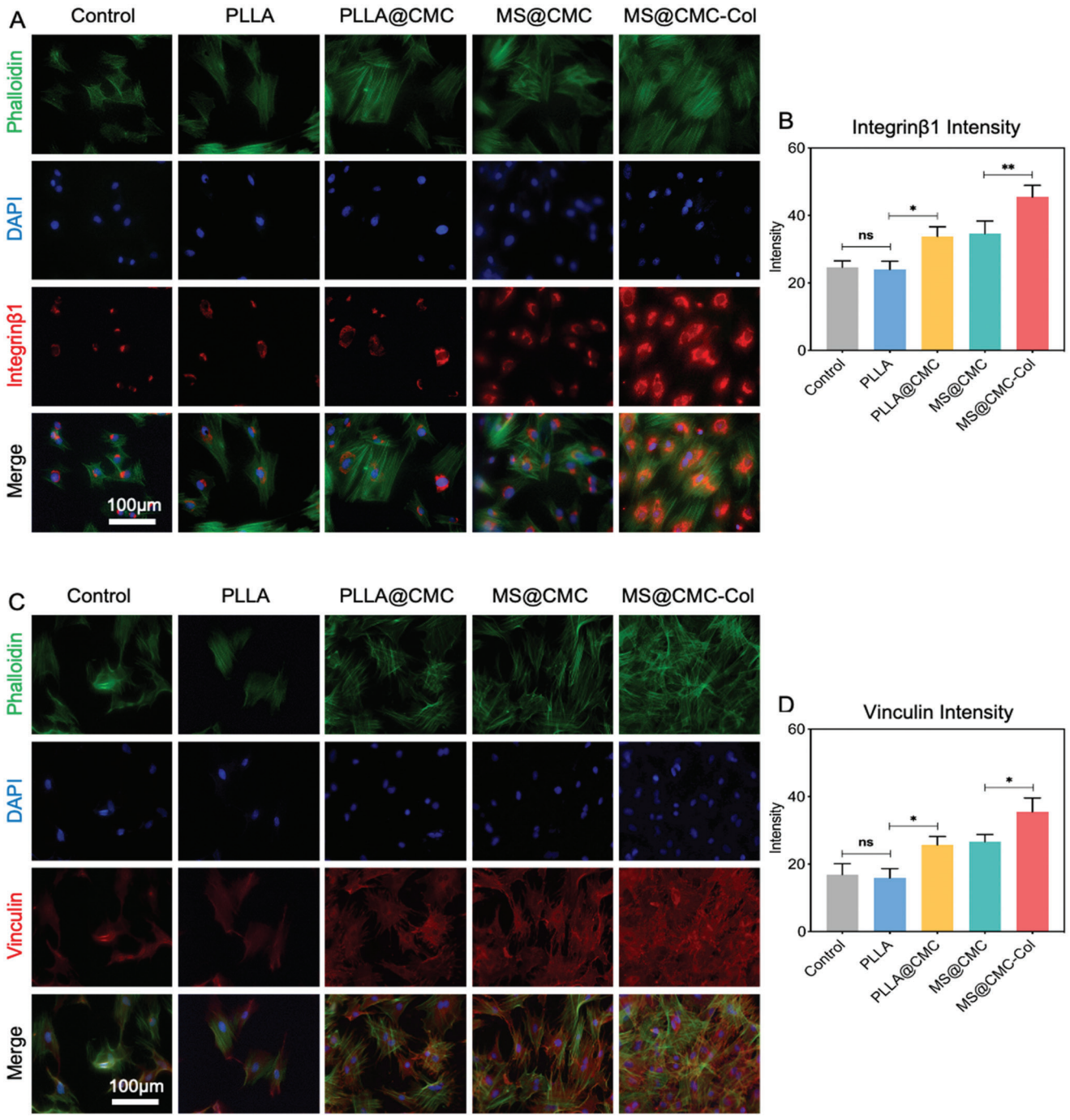

Figure 2. Mechanism of cell adhesion. A) Immunofluorescence staining of integrin $\beta 1$. B) Fluorescence intensity of integrin $\beta 1$. C) Immunofluorescence staining of vinculin. D) Fluorescence intensity of vinculin. (Statistical analysis entails one-way ANOVA followed by Tukey's multiple comparison test; $n = 3$; ns, not statistically significant; $^{*}p < 0.05$; $^{**}p < 0.01$.)

and M2 can regulate bone regeneration by reconstructing the immune microenvironment through the secretion of different cytokines.[31] To assess the controlled modulation of Mφ polarization by the bionic periosteum, Mφ cocultured with different electrospun fibers were collected and evaluated for their phenotypes. Flow cytometry analysis after 3 d of coculture (**Figure 3**A–C) Mφ on different electrospun fibers revealed a high percentage of $CD11b^{+}/CD86^{+}$ cells and a low expression of $CD11b^{+}/CD206^{+}$, in all groups. After 7 d of coculture (Figure 3D–F), the expression of $CD11b^{+}/CD86^{+}$ in all groups decreased, while the expression of $CD11b^{+}/CD206^{+}$ increased in all groups. From a comparison of the PLLA@CMC and MS@CMC groups, the $CD11b^{+}/CD206^{+}$ ratio of scaffold-incorporated IL-4 was significantly higher than that of the scaffold without

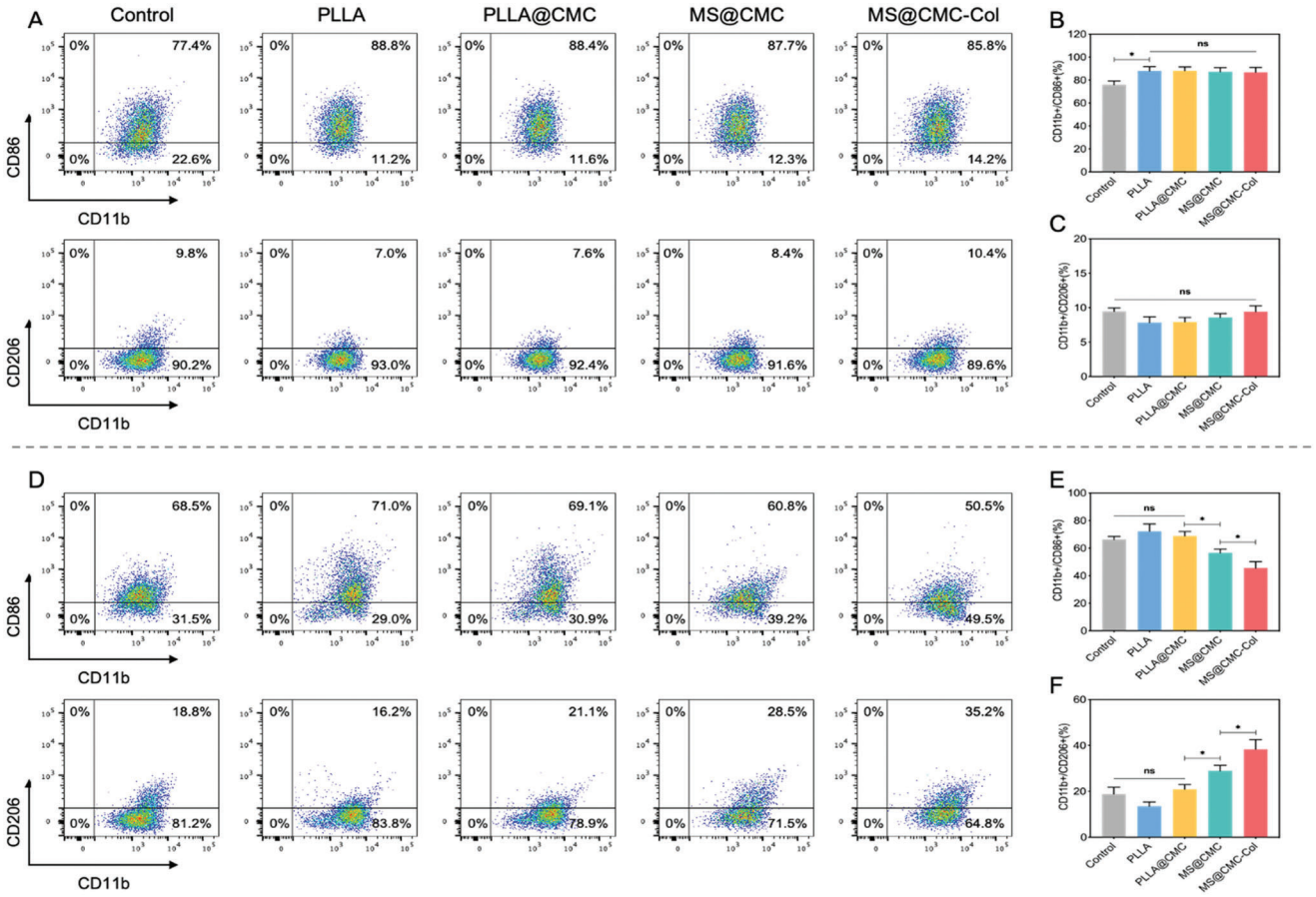

Figure 3. FCA result of polarization on Mφ. A,D) Expressions of CD86 and CD206 in Mφ at 3 and 7 d by flow cytometry. B,C) Quantitative analysis of the result of flow cytometry at 3 d. E,F) Quantitative analysis of FCA at 7 d. (Statistical analysis entails one-way ANOVA followed by Tukey's multiple comparison test; $n = 3$; ns, not statistically significant; $^*p < 0.05$.)

IL-4. After adding collagen, the $CD11b^+/CD206^+$ ratio in the MS@CMC-Col group was significantly higher than that in the MS@CMC group, reaching 35.2%. Therefore, Col-I indeed influenced the macrophage response and cooperated with IL-4 to promote M2 polarization.[32] The same results were observed in cellular immunofluorescence staining, where almost all cells in each group were stained with green fluorescence of F4/80, a surface marker of Mφ. After 3 d of coculture, cells in each group were stained with strong red fluorescence representing INOS, a surface marker of the M1 subtype (**Figure 4**A). Moreover, fluorescence representing CD206, a surface marker of M2 subtype intensity, was weak in all groups (Figure 4B). In contrast, after 7 d of coculture, INOS fluorescence was significantly weaker in MS@CMC-Col than in other groups (Figure 4C), while fluorescence of CD206 was significantly stronger in MS@CMC-Col than in other groups (Figure 4D), and cells on MS@CMC-Col had a more elongated morphology with more pseudopods than cells in other groups. The same trend was revealed in the semiquantitative analysis of the fluorescence corresponding to INOS and CD206 after 3 and 7 d of coculture (Figure 4E–H). Combined with the above phenotypic analysis, we can conclude that a small amount of IL-4 released from the bionic periosteum in the first 3 d does not affect the polarization of Mφ toward M1. Additionally, after 3 d, the massive release of IL-4 from the gel phase promotes the polarization of Mφ towards M2 for bone regeneration.

The cell culture medium of Mφ cocultured on different electrospun fibers was collected to quantify the relevant inflammatory cytokines using ELISA kits. After 3 d of coculture, the secretion of TNF-α, a pro-inflammatory factor, was significantly higher than that of IL-10, an anti-inflammatory factor, in all groups (Figure S7, Supporting Information), and the differences in the secretion of TNF-α and IL-10 among all groups were not statistically significant. After 7 d, the secretion of TNF-α decreased and the secretion of IL-10 increased significantly in all groups. The secretion of IL-10 in MS@CMC-Col was significantly higher than that of other groups. The results indicated that a slight release of IL-4 during the first 3 d would not affect the establishment of a moderate inflammatory microenvironment, while the massive release of IL-4 after 3 d significantly promoted remodeling of the anti-inflammatory microenvironment for bone regeneration.

To further verify the changes in the phenotype and function of Mφ, qRT-PCR was performed on the cells for a genomic analysis (Figure 4I–L). After 3 d of coculture with different electrospun fibers, the expressions of INOS and TNF-α in Mφ were significantly increased, while the expressions of Arg-1 and IL-10 were low in all groups. After 7 d, the expressions of INOS and TNF-α

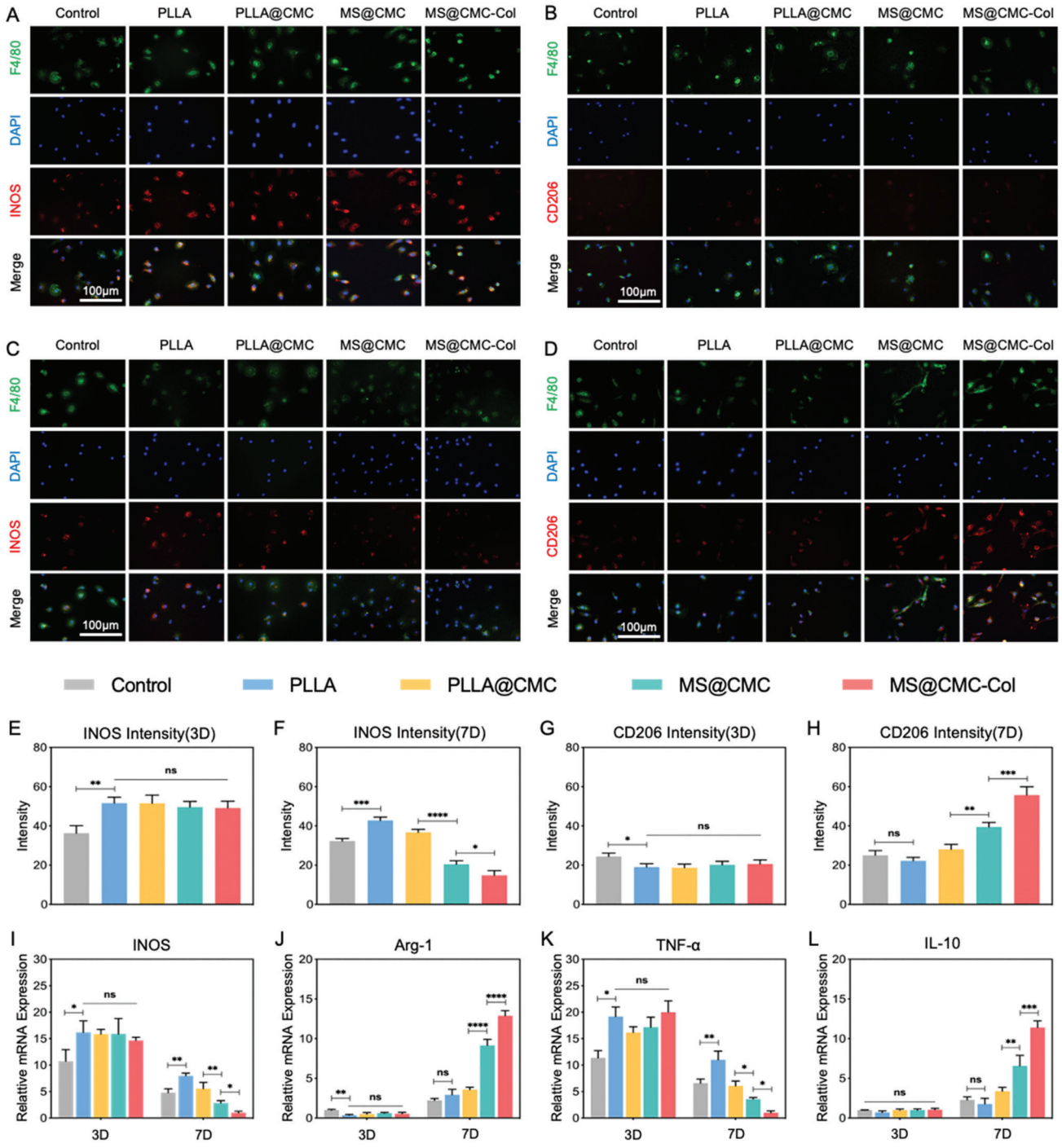

Figure 4. IF and PCR analysis of polarization on Mφ. A,C) Immunofluorescence staining of F4/80 and INOS at 3 and 7 d. B,D) Immunofluorescence staining of F4/80 and CD206 at 3 and 7 d. E,F) Fluorescence intensity of INOS at 3 and 7 d. G,H) Fluorescence intensity of CD206 at 3 and 7 d. I–L) Expression analysis of inflammatory genes INOS, Arg-1, TNF-α, and IL-10 at 3 and 7 d. (Statistical analysis entails one-way ANOVA followed by E–H) Tukey's multiple comparison test and two-way ANOVA followed by I–L) Tukey's multiple comparison test; $n = 3$; ns, not statistically significant; $^{*}p < 0.05$; $^{**}p < 0.01$; $^{***}p < 0.001$; $^{****}p < 0.0001$.)

decreased in all groups, and the expressions of Arg-1 and IL-10 were upregulated. In the MS@CMC-Col group, the expressions of Arg-1 and IL-10 were significantly increased compared with that in the other groups. The results further demonstrated that the biphasic bionic periosteum could promote the polarization of Mφ towards M2 during the anti-inflammatory repair phase by its controlled IL-4 release.

To better understand the molecular mechanisms by which the biphasic bionic periosteum promoted the polarization of Mφ towards M2, Mφ were collected after 7 d of coculture with

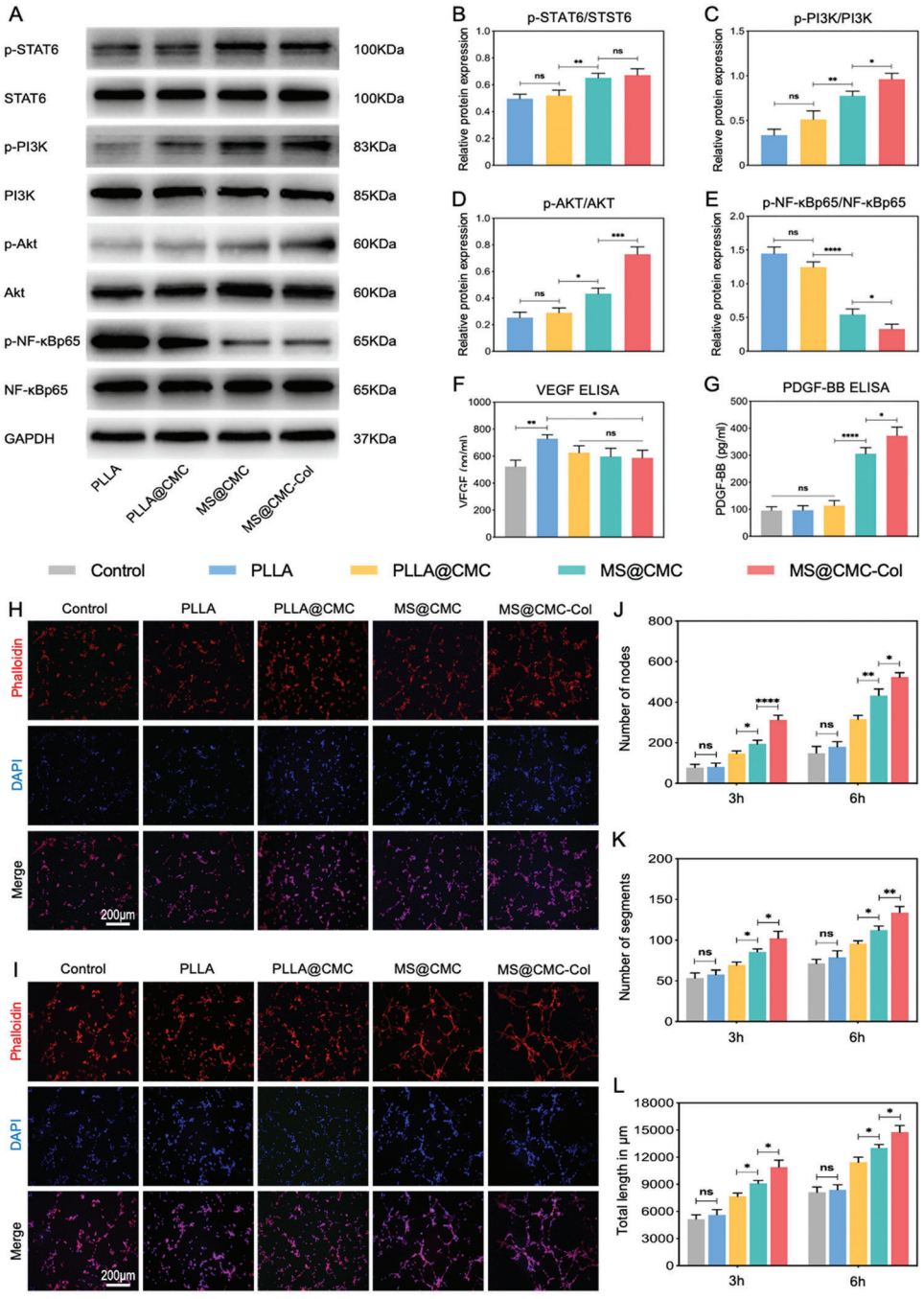

Figure 5. Mechanism of polarization on Mφ and angiogenic paracrine on HUVECs. A) Phosphorylation levels of STAT6, PI3K, AKT, and NFκbp65 by western blotting. B–E) Quantitative analysis of phosphorylation levels of STAT6, PI3K, AKT, and NFκbp65. F,G) Detection of VEGF and PDGF-BB secreted by Mφ through ELISA. H–I) Fluorescence staining of HUVEC vascularization under different electrospun fibers/Mφ conditions. J–L) Quantitative analysis of number of nodes, number of segments, and total length. (Statistical analysis entails one-way ANOVA followed by B–G) Tukey's multiple comparison test and two-way ANOVA followed by J–L) Tukey's multiple comparison test; $n = 3$; ns, not statistically significant; *$p < 0.05$; **$p < 0.01$; ***$p < 0.001$; ****$p < 0.0001$.)

different electrospun fibers and analyzed by western blotting (WB) to examine the two major signaling pathways that activate the polarization of Mφ toward M2: JAK/STAT-6 and PI3K/Akt/NF-κB.[33] The results of WB (**Figure 5**A) and quantitative analysis (Figure 5B–E) showed that the expressions of p-STST6/STAT6 in MS@CMC and MS@CMC-Col were increased compared with that in the other groups. Therefore, IL-4 released from the fiber phase of the bionic periosteum activated JAK by binding to IL-4R on the surface of Mφ, thereby mediating STAT6 phosphorylation to trigger the polarization of

Mφ towards M2. In contrast, the expressions of p-PI3K/PI3K and p-AKT/AKT in MS@CMC and MS@CMC-Col were also significantly higher than that in the other groups, while the expression of p-NF-κBp65/NF-κBp65 was significantly lower than that in other groups. The results confirmed that the bionic periosteum inhibited the activation of inflammatory signal NF-κBp65 via PI3K/AKT signaling, thus promoting the polarization of Mφ towards M2.

In summary, the biphasic bionic periosteum can actively coordinate Mφ polarization through the controlled release of IL-4 to maintain a moderate inflammatory microenvironment at the early inflammatory phase while promoting the polarization of Mφ towards M2 for tissue repair during the anti-inflammatory repair phase and removing the inhibition of the spontaneous conversion of macrophages. Cytokines secreted by Mφ greatly improve the local osteogenic microenvironment, thereby promoting bone regeneration.

2.2.4. Moderate Inflammatory Microenvironment Constructed by M1 Macrophage for Recruiting BMSCs

The migration of BMSCs is initiated by SDF-1 secreted by M1 macrophages.[34] Therefore, the transwell chemotactic migration assay was used to evaluate the moderate immune microenvironment in the early stage of inflammation under the immune regulation of fibrous membranes. As shown in Figure S8 (Supporting Information), owing to the early sudden release of IL-4, the number of cells recruited by MS and MS-Col was considerably lower than that recruited by fibrous membranes with controlled release of IL-4, which provided sufficient seed cells for bone repair.

2.2.5. Vascularization Promoted by Biphasic Bionic Periosteum

Vascular regeneration in bone healing is extremely important, and Mφ participate in the germination and maturation of neovascularization through paracrine-related cytokines.[35] The effects of controlled regulation of macrophage polarization by the bionic periosteum on angiogenesis were investigated. The expressions of vasoactive factors were investigated using ELISA kits (Figure 5F,G), revealing that there was no significant difference in the expression level of VEGF in different electrospun fibers. Moreover, the expression of VEGF in PLLA was slightly higher than that in MS@CMC-Col, while the expression of PDGF-BB in MS@CMC-Col was significantly higher than that of other groups. M1 mainly secreted VEGF to promote early vascular neogenesis, while M2 secreted cytokines such as PDGF-BB and MMP-9 to promote vascular maturation and remodeling. To further explore this complex process, angiogenesis experiments were performed on HUVECs. After 3 h (Figure 5H) and 6 h (Figure 5I) of culture, HUVECs in PLLA, PLLA@CMC, and MS@CMC-Col showed only a small number of tubular structures, while HUVECs in MS@CMC-Col formed many vascular networks with primitive reticular structures spreading in all directions. Quantitative analysis of the number of nodes (Figure 5J), number of segments (Figure 5K), and total length (Figure 5L) of the tubular structures revealed that, after 6 h of culture, the number of nodes, number of segments, and total length of MS@CMC-Col were respectively 524.3 ± 7.0, 125.3 ± 6.5, and 14705.0 ± 391.0 μm, which were significantly higher than those of the other groups. Although M1 secreted more VEGF to act on early neovascular sprouting, factors secreted by M2 such as PDGF-BB to promote vascular maturation and remodeling were apparently more important.

In vitro angiogenesis experiments further demonstrated that the biphasic bionic periosteum could improve the local microenvironment by controlled regulation of macrophage polarization to promote endothelial cell migration, vascular sprouting, and maturation, thereby promoting metabolite transport and local tissue metabolism and reducing local ischemia and hypoxia, ultimately promoting bone regeneration.

2.2.6. Osteogenesis Promoted by Biphasic Bionic Periosteum

The immune response is initiated immediately after the occurrence of a bone defect, and relevant immune cells accumulate at the defect and start to secrete relevant cytokines to recruit stem cells, which are regulated by the local microenvironment to further proliferate and differentiate for tissue regeneration.[6a] As an important member in the first line of immune defense, Mφ account for approximately 20% of all bone marrow cells at the defect site. Cytokines required for the proliferation and osteogenic differentiation of BMSCs can be secreted by Mφ. The expressions of osteogenic-related cytokines by Mφ were determined using ELISA kits. The results (**Figure 6**A,B) showed that MS@CMC-Col significantly upregulated the expressions of BMP-2 and TGF-β1, which positively regulated the osteogenic process by activating related signaling pathways. To further investigate the effect of the local microenvironment formed by osteogenic cytokines secreted by M2 on the osteogenic differentiation of BMSCs, transwell plates were used to coculture Mφ and BMSCs with different electrospun fibers.

Alkaline phosphatase (ALP) secreted by osteoblasts can directly reflect the activity and function of osteoblasts and is a marker of early osteoblast differentiation and bone mineralization. After 7 d of coculture in transwell chambers, BMSCs were collected for ALP staining and activity assay. MS@CMC-Col had significantly deeper ALP staining and better cell morphology than other groups (Figure 6C). Although the ALP staining of MS@CMC was deeper than that of PLLA and PLLA@CMC, there was still a big gap compared with MS@CMC-Col (Figure 6D). This may be attributed to the presence of Col-I on the surface of MS@CMC-Col, which plays an important role in osteogenic differentiation and mineralization of BMSCs.

Osteocalcin (OCN), a calcium-binding protein synthesized and secreted by mature osteoblasts, is a major component of bone non-collagenous proteins and is considered a marker of osteoblast differentiation toward the mineralization phase because it occurs mainly during the mineralization formation phase.[36] BMSCs were collected after 14 d of coculture in transwell chambers for immunofluorescence staining of OCN. BMSCs on different electrospun fibers grew well but showed varying degrees of osteogenic differentiation (Figure 6E). BMSCs on MS@CMC-Col presented the most intense of red fluorescence representing OCN and better spreading of cells among all groups. This was

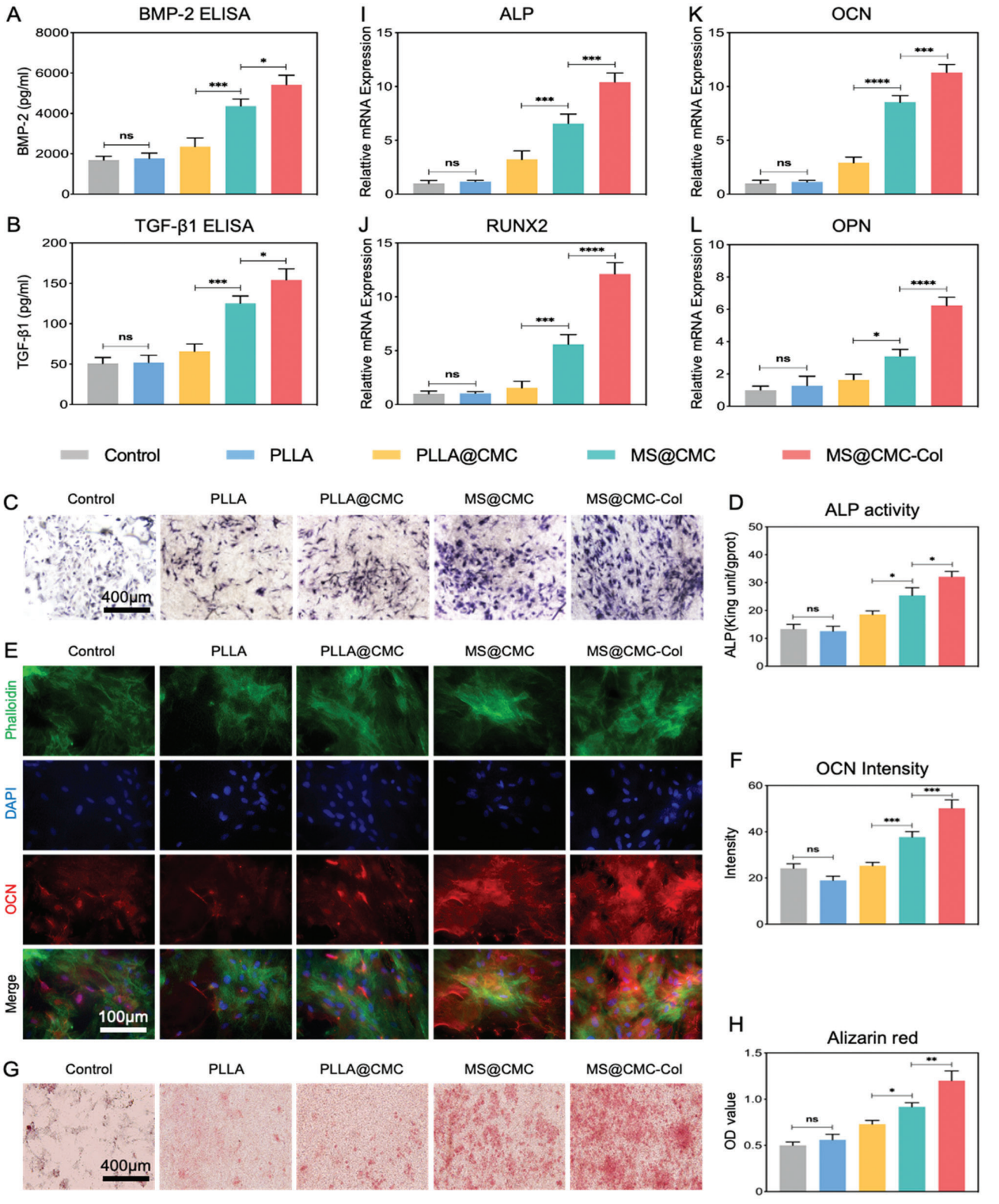

Figure 6. Evaluation of osteogenesis under coculture conditions. A,B) Detection of BMP-2 and TGF-β1 secreted by Mφ through ELISA. C) Light micrographs of ALP staining. D) Quantitative assay of ALP activity. E) Immunofluorescence staining of OCN. F) Fluorescence intensity of OCN. G) Light micrographs of alizarin red staining. H) Detection of calcium nodules. I–L) Expressions of osteogenesis-related genes of ALP, RUNX2, OCN, and OPN. (Statistical analysis entails one-way ANOVA followed by Tukey's multiple comparison test; $n = 3$; ns, not statistically significant; *$p < 0.05$; **$p < 0.01$; ***$p < 0.001$; ****$p < 0.0001$.)

corroborated in the semi-quantitative analysis of immunofluorescence staining of OCN (Figure 6F).

Calcium nodules, a mineralized extracellular matrix formed by osteoblasts, indicate the final stage of osteogenic differentiation. BMSCs were collected after 21 d of co-culture in transwell chambers for alizarin red staining. The calcium nodules in MS@CMC-Col were the most abundant and compact among all groups (Figure 6G). Quantitative analysis of the calcium nodules (Figure 6H) produced results that were consistent with the staining results. The collagen component on the surface of MS@CMC-Col enhanced the mineralization of BMSCs, and thus calcium salts were continuously deposited in the extracellular matrix, endowing the bionic periosteum with excellent osteogenesis and bone mineralization ability in the late stage of osteogenesis.

To further verify the ability of the biphasic bionic periosteum to promote the osteogenic differentiation of BMSCs, qRT-PCR was used to evaluate the expression of genes related to osteogenic differentiation. ALP and Runx2, which represent early osteogenic differentiation of cells, and OCN and OPN, which represent late osteogenic differentiation of cells, were detected. Under the controlled immunomodulation of MS@CMC-Col, BMSCs showed excellent osteogenic ability, both for early and late osteogenic indexes (Figure 6I–L).

Overall, MS@CMC-Col regulated the polarization of Mφ towards M2 through the controlled release of IL-4 from the fiber phase during the anti-inflammatory repair stage. Additionally, the immune microenvironment reconstituted by M2 coordinated with the excellent mineralization and osteogenic activity in the gel phase to promote the osteogenic differentiation of BMSCs.

In summary, MS@CMC-Col biphasic bionic periosteum with controlled release of IL-4 exhibited excellent biological properties in vitro. The gel phase endowed the bionic periosteum with excellent biocompatibility, cellular adhesion, and mineralization ability and provided support for seed cells to perform biological functions in the long term. The moderate inflammatory response of M1 macrophage improved the recruitment of BMSCs and vascular sprouting in the early stage of inflammation. Synergy between the controlled release of IL-4 loaded in the fiber phase and Col-I promoted the polarization of Mφ towards M2 in the anti-inflammatory repair stage, and M2 cooperated with endogenous cells like BMSCs and HUVECs to regulate the BIM through paracrine, thus improving angiogenesis and osteogenic differentiation.

2.3. In Vivo Experiments

To investigate the effects of the biphasic bionic periosteum on bone regeneration in vivo, 5 mm critical bone defects were constructed in rat models (Figure S9, Supporting Information). Different electrospun fibers were implanted on the bone defects. Cranial specimens were collected at 3 and 7 d after surgery to assess the local immune microenvironment of the bone defect, and cranial specimens were collected at 4 and 8 weeks after surgery to analyze the bone repair.

2.3.1. BIM Modulation

In the early phase of inflammation after acute bone injury, neutrophils first arrive at the injury site and secrete relevant cytokines and chemokines to recruit Mφ, which then begin to dominate, switch phenotype, and function in response to changes in the microenvironment as local injury and inflammation are brought under control.[34b] The successful conversion of Mφ in response to the controlled release of IL-4 from the bionic periosteum is relevant to the outcome of bone regeneration. Immunofluorescence images and semiquantitative analysis of these images (**Figure 7**A,E,F) revealed that the green fluorescence of INOS, representing M1, was strong in all groups of electrospun fibers, while the red fluorescence of Arg-1, representing M2, was weak in all groups of electrospun fibers at 3 d after surgery. In contrast, at 7 d after surgery (Figure 7B,G,H), the red fluorescence of Arg-1 in the MS@CMC-Col group was significantly stronger than that of other groups of electrospun fibers, and the Arg-1 fluorescence was significantly stronger than the INOS fluorescence. Moreover, the green fluorescence in the groups of electrospun fibers except MS@CMC-Col was maintained a certain intensity, which was significantly weaker than that at 3 d after surgery. The results indicated that MS@CMC-Col not only promoted the polarization of Mφ towards M2 at the middle and late stages of inflammation but also did not affect the polarization of Mφ toward M1 at the early stage of inflammation. Similar phenotype changes were observed in the immunofluorescence staining of TNF-α and IL-10 with semi-quantitative analysis at 3 d (Figure 7C,I,J) and 7d (Figure 7D,K,I) after surgery. The expression of inflammatory factor TNF-α was high in all groups and the expression of anti-inflammatory factor IL-10 was low in all groups at 3 d after surgery, while the expression of TNF-α was significantly decreased and the expression of IL-10 was significantly increased in MS@CMC-Col at 7 d after surgery. These results revealed that MS@CMC-Col successfully promoted the polarization of Mφ towards M2 during the anti-inflammatory repair phase of the bone-repair process and effectively improved the BIM.

2.3.2. Evaluation of Bone Repair

Micro-CT scans of the collected specimens were reconstructed to evaluate bone repair. Reconstructed images of the bone defects (**Figure 8**A) showed that bone repair by MS@CMC-Col was significantly better than that by the other groups, at 4 and 8 weeks after surgery. There was a small amount of newly formed bone around the defect in the control group owing to the lack of scaffold protection and osteoconduction. There was slightly better bone repair in the group of PLLA due to the presence of PLLA scaffold, but a small gap with PLLA@CMC remained. MS@CMC and MS@CMC-Col both promoted better bone repair than the other groups of electrospun fibers without IL-4. MS@CMC-Col promoted the most superior bone repair among the groups of electrospun fibers owing to the presence of Col-I on the surface, which synergistically promoted cell adhesion and mineralization. Unlike the edge-to-center repair pattern in the control and PLLA groups, gel-coated electrospun fibers induced direct intramembranous osteogenesis at any location, suggesting that gel-coated electrospun fibers have the same biological function as the natural periosteum to promote bone regeneration. Quantitative analysis of micro-CT images showed that, at the same time point, bone volume/tissue

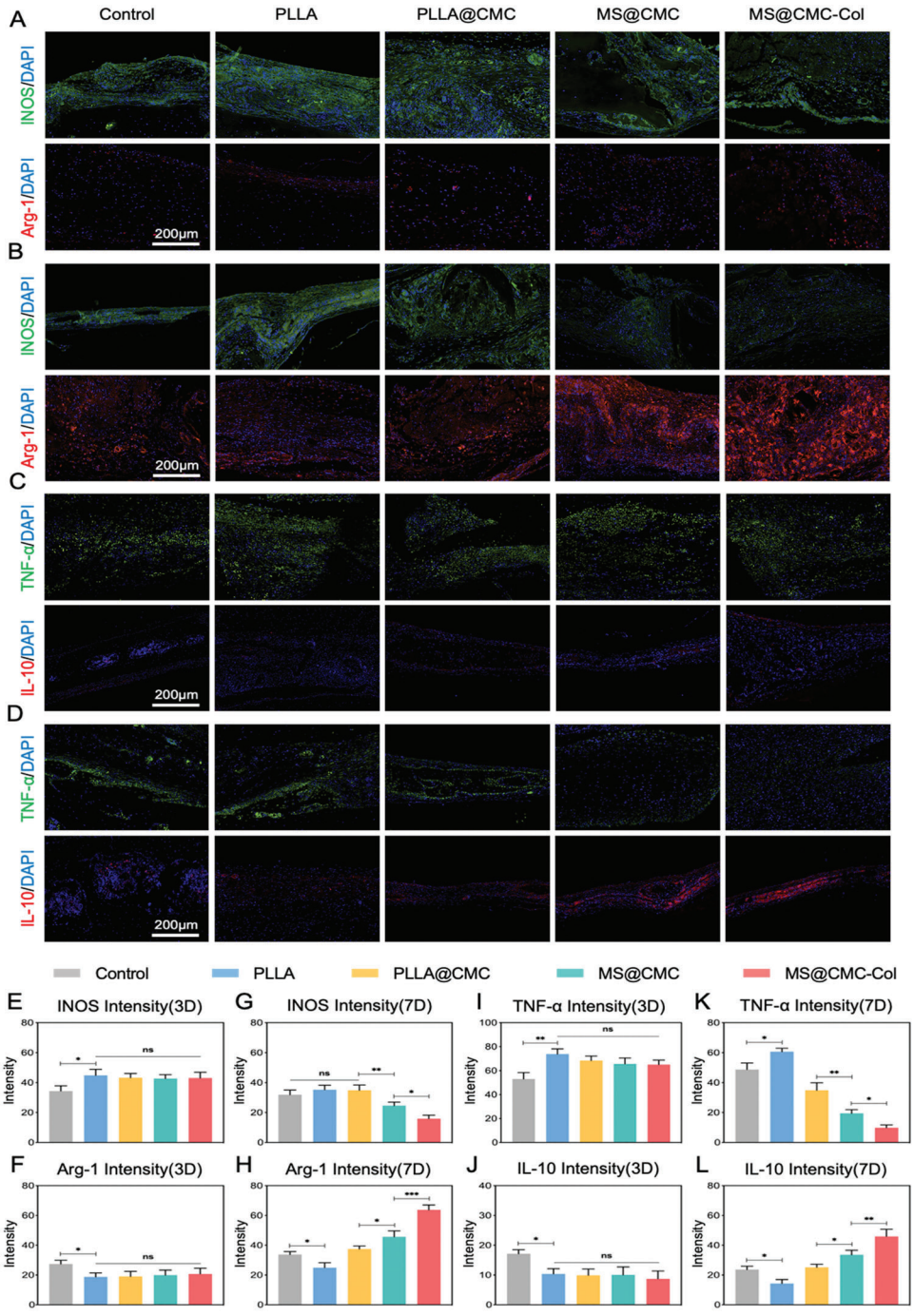

Figure 7. Biphasic bionic periosteum modulates the osteogenic immune microenvironment in vivo. A) Immunofluorescent staining of INOS and Arg-1 at 3 d. B) Immunofluorescent staining of INOS and Arg-1 at 7 d. C) Immunofluorescent staining of TNF-α and IL-10 at 3 d. D) Immunofluorescent staining of TNF-α and IL-10 at 7 d. E,F) Fluorescence intensity of INOS and Arg-1 at 3 d. G,H) Fluorescence intensity of INOS and Arg-1 at 7 d. I,J) Fluorescence intensity of TNF-α and IL-10 at 3 d. K,L) Fluorescence intensity of TNF-α and IL-10 at 7 d. (Statistical analysis entails one-way ANOVA followed by Tukey's multiple comparison test; $n = 5$; ns, not statistically significant; $^{*}p < 0.05$; $^{**}p < 0.01$; $^{***}p < 0.001$.)

volume (BV/TV) (Figure 8B), bone mineral density (BMD) (Figure 8C), and bone surface (BS) repair ratio (Figure 8D) were higher in all groups of electrospun fibers than those in the control group, and MS@CMC-Col had the best values among all groups.

Histological analysis of cranial bone specimens was carried out. H&E staining (**Figure 9**A) results showed that bone repair was better in all groups of electrospun fibers than that in the control group, and among all groups of electrospun fibers, the MS@CMC-Col group presented the highest values of quantity,

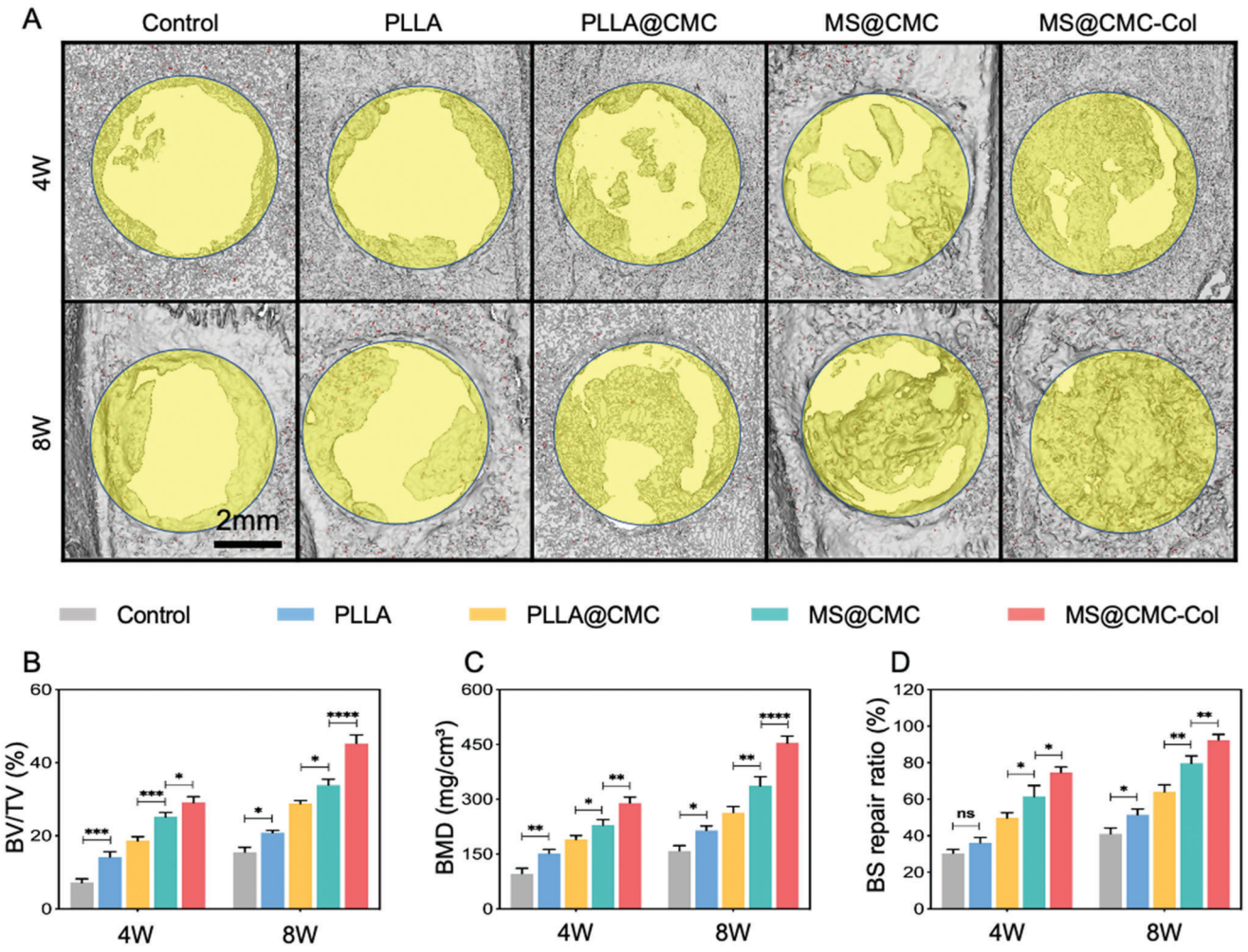

Figure 8. Radiological assessment of osteogenic effect in vivo. A) Surface reconstruction of micro-CT of the cranial defect area. B) Bone volume fraction (BV/TV). C) Bone mineral density (BMD) in the bone defect area. D) Repair ratio of bone surface (BS). (Statistical analysis entails two-way ANOVA followed by Tukey's multiple comparison test; $n = 5$; ns, not statistically significant; *$p < 0.05$; **$p < 0.01$; ***$p < 0.001$; ****$p < 0.0001$.)

volume, and continuity of bone tissue at 4 and 8 weeks after surgery. These results were confirmed with quantitative histological analysis of new bone (Figure 9B,C).

Masson staining was used to evaluate the maturity of new bone tissue, especially during bone defect repair from crustal neogenesis to mature remodeling. The deeper the red stain, the more mature the crust. Red-blue interdigitated staining revealed that new bone tissues were formed at bone defects in all groups (Figure 9D). There were larger, sheet-like red-stained areas with better continuity in the MS@CMC-Col group, consistent with the results of the quantitative analysis of red-stained areas (Figure 9E,F). Immunohistochemical staining for OCN (**Figure 10**A,D,E), an indicator of late osteogenic differentiation of cells, revealed that the positive expression of OCN in the MS@CMC-Col group was significantly higher than that in the other groups, suggesting excellent bone repair.

Neovascularization is the source of nutrition at the bone defect. Thus, early vascularization is important for bone regeneration and regulation of the immune microenvironment.[37] During bone regeneration, Mφ secrete vasoactive factors to promote the sprouting and maturation of neovascularization. Platelet endothelial cell adhesion molecule (CD31), which is highly expressed on endothelial cells as an adhesion molecule in the immunoglobulin superfamily, is often used to assess vascular regeneration.[38] Immunohistochemical staining for CD31 (Figure 10B,F,G) revealed a large amount of neovascularization, labeled as brown, round, or oval by CD31 antibody, in the vicinity of bone defects in the MS@CMC-Col group at 4 and 8 weeks after surgery. As the peak of angiogenesis would shrink over time from 2 weeks after surgery, MS@CMC-Col showed better early angiogenic capacity at four weeks, while the number of blood vessels showed an overall decreasing trend in defect area at eight weeks. Overall, the biphasic bionic periosteum can promote neovascularization by modulating the immune microenvironment to promote the secretion of cytokines such as VEGF and PDGF-BB.

Periostin is an extracellular matrix protein that is specifically expressed in the periosteum and periodontal tissues. Periostin in the periosteum is mainly secreted by preosteoblasts and regulates the adhesion, migration, and differentiation of osteoblasts.[39] Periostin can be used as a specific marker of the periosteum because

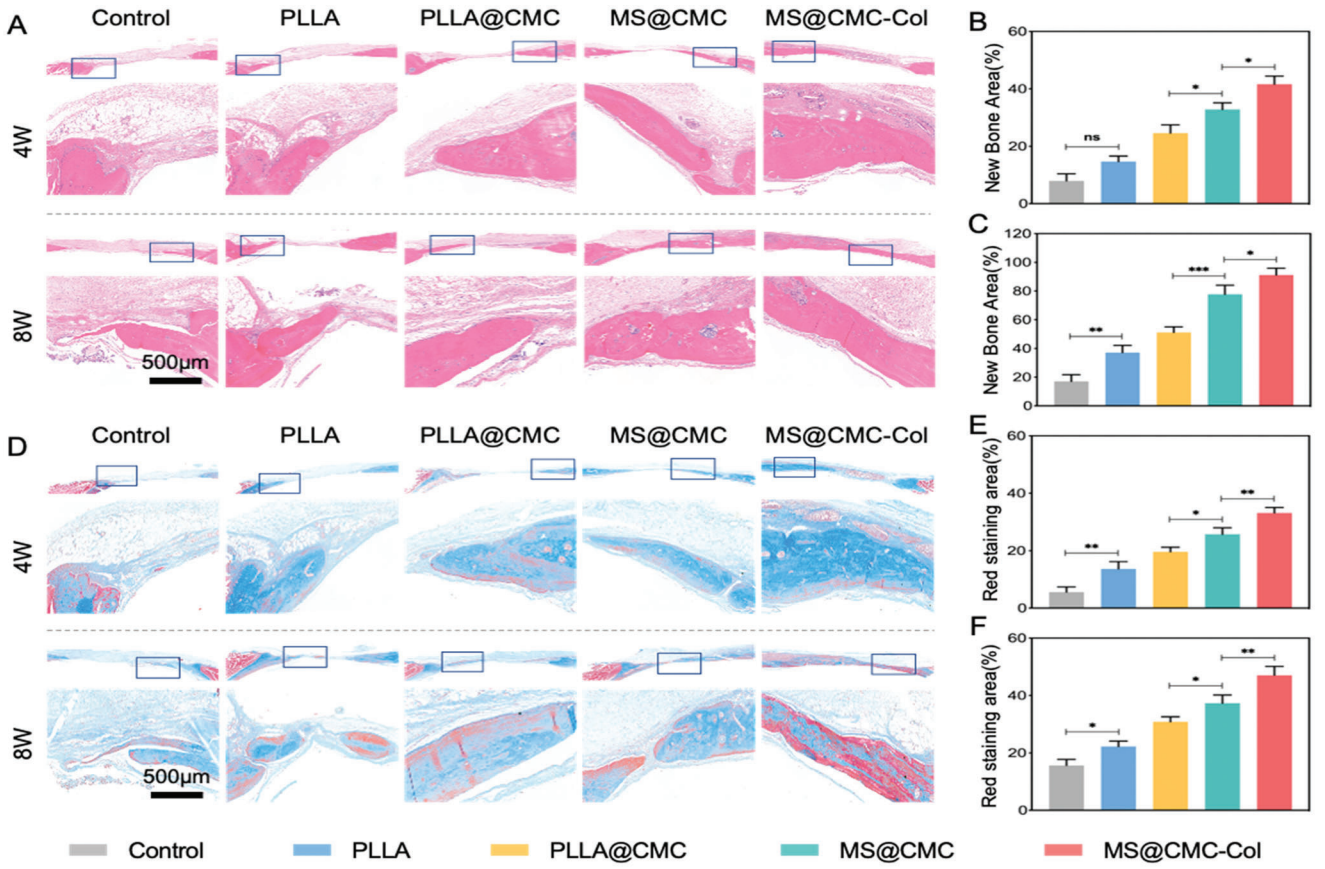

Figure 9. Histological assessment of osteogenic effect in vivo. A) H&E staining of the cranial defect at 4 and 8 weeks. B,C) Quantitative analysis of the new bone at 4 and 8 weeks. D) Masson staining of the cranial defect at 4 and 8 weeks. (E, F) Quantitative analysis of Masson staining (red-stained areas) at 4 and 8 weeks. (Statistical analysis entails one-way ANOVA followed by Tukey's multiple comparison test; $n = 5$; ns, not statistically significant; $^{*}p < 0.05$; $^{**}p < 0.01$; $^{***}p < 0.001$.)

it is specifically expressed therein.[40] Immunohistochemical results (Figure 10C,H,I) revealed that periostin was formed on the surface of the new bone and arranged linearly along the bone tissue in the MS@CMC-Col group, in contrast to the disordered and scattered distribution of periostin in the other groups, demonstrating the ability of the biphasic bionic periosteum to promote bone regeneration and periosteal repair.

In summary, the biphasic bionic periosteum demonstrated excellent immunomodulatory function and osteogenic-vascular activity in vivo through controlled release of IL-4 to modulate the BIM and structural properties of mimicking the natural periosteum, leading to sustainable bone regeneration.

At present, most artificial periostea have the disadvantage of a single structure and lack the "active" ability to regulate the inflammatory environment after implantation. The biphasic bionic periosteum prepared in our study not only has heterogeneous components (fiber phase and gel phase) and structural integration (collagen self-assembly and GP covalent crosslinking) but also can sequentially regulate the immune microenvironment. The fiber phase is used to load and protect IL-4 as well as to provide the main mechanical support. The gel phase is tightly filled in the pores and surface of the fiber phase, which not only improves the biocompatibility and adhesion of the bionic periosteum but also effectively suppresses the initial sudden release of IL-4 from the fiber phase to maintain the moderate inflammatory response of M1 macrophages for mesenchymal stem cell recruitment and vascular sprouting on day 3. The cumulative effect of M2 polarization induced by the large amount of IL-4 released from the fibrous phase and the presence of Col-I in the bionic periosteum leads to an anti-inflammatory immune microenvironment on day 7, which promotes osteogenic differentiation and vascular maturation. Thus, the bionic periosteum achieves sequential regulation of the microenvironment to promote bone regeneration.

3. Conclusion

In this study, a hydrogel-electrospun biphasic bone periosteum was constructed to modulate the BIM accurately. By coating the surface of IL-4 loaded micro-sol electrospun fibers with a compact CMC-Col hydrogel, the biphasic bionic periosteum not only emulated the natural periosteum for cell adhesion, proliferation, and differentiation but also acted as a dam to intercept the burst release of IL-4. As a result, the moderate inflammatory response of M1 macrophage for mesenchymal stem cell recruitment and vascular sprouting at the acute fracture was maintained. IL-4 released during the anti-inflammatory repair stage cooperated with Col-I to promote the polarization of Mφ towards M2. A BIM

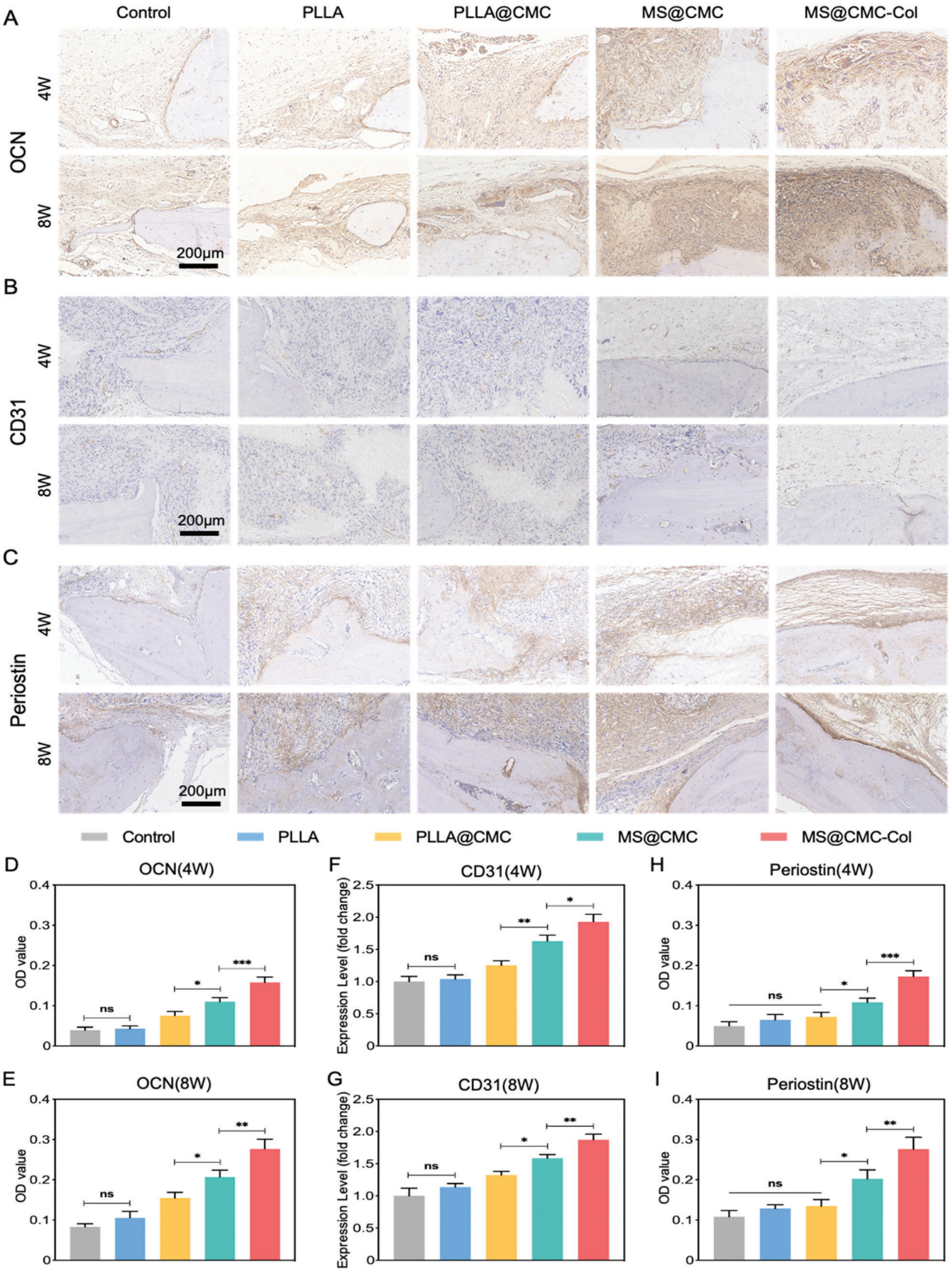

more suitable for the proliferation and differentiation of cells like BMSCs, osteoblasts, and HUVECs was constructed by the osteogenic, angiogenic, and related anti-inflammatory factors produced by M2, thus promoting bone regeneration. However, further study is needed to adjust the dosage of CMC, Col, and GP to achieve programmed release via the gel coating. Overall, the composite fiber scaffold constructed in this study, which sequentially regulates the immune response, provides a biomaterial therapy strategy to coordinate the immune microenvironment and bone regeneration for the repair of bone defects.

4. Experimental Section

Preparation of PLLA and MS Electrospun Fibers: 0.5 g of PLLA (Idle Gang, Jinan, China) was added to 4 g of dichloromethane (DCM) (Aladdin, Shanghai, China). PLLA was dissolved completely in DCM at room temperature using a magnetic stirrer to obtain a viscous and homogeneous solution. Then, 2 g of *N,N*-dimethylformamide (DMF) (Qiang Shun, Shanghai, China) was added to obtain a PLLA solution for electrospinning. 0.1 g of hyaluronic acid (HA) (Yuancheng, Wuhan, China) was added to 9.9 g of deionized water and stirred well at room temperature to obtain 1 wt% HA aqueous solution. Subsequently, 10 µL of IL-4 (100 µg mL^{-1}) (Peprotech, USA) was mixed thoroughly with 50 µL of 1 wt% HA solution to obtain a homogeneous 1% HA-IL-4 aqueous solution. Then, 0.01 g of Span 80 (Sigma, USA) and 4 g DCM were mixed and stirred well at room temperature, and 0.5 g of PLLA and 2 g of DMF were mixed and stirred well to obtain the micro-sol electrospinning solution.

The electrospinning solution was inserted into a 10 mL sterile syringe, which was attached to a blunt-tipped syringe steel needle with an inner diameter of 0.9 mm and fixed on a precision propulsion pump (Lange, Baoding, China). One end of the DC high voltage power supply (Dongwen, Tianjin, China) was attached to the steel needle syringe tip at 5 mm, and the other end was attached to a cylindrical drum receiver wrapped with aluminum foil. The receiver was parallel to the tip of the needle and the distance was approximately 15 cm. The propulsion pump rate was set to 70 µL min^{-1}, the receiver rate was set at 120 rpm, and the voltage was set to approximately 15 kV. The prepared electrospun fibers were dried overnight in a vacuum oven to remove residual organic solvents, and named PLLA or MS.

Construction of CMC and CMC-Col Hydrogel Coatings: The PLLA and MS electrospun fibers were first hydrated in 75% ethanol for 30 min. Thereafter, 0.1 g of CMC (Aladdin, Shanghai, China) and 0.01 g of GP (Zhixin, Sichuan, China) were configured into 10 mg mL^{-1} of aqueous solution, and 10 mL of CMC solution and 1 mL of GP solution were mixed well in a water bath set to 50 °C. Then, the mixed solution was uniformly dropped on PLLA or MS electrospun fibers and placed in a thermostat set to 37 °C overnight to assemble the prepared fibrous membranes, named PLLA@CMC or MS@CMC, respectively.

Col-I (Sigma–Aldrich, USA) was dissolved in 0.1 M acetic acid solution (QiangSheng, Jiangsu, China) to form a collagen solution with a final concentration of 3 mg mL^{-1} and then stored at 4 °C. The collagen solution was mixed and diluted with 10× phosphate-buffered saline (PBS) in the ratio of 1:6, and the pH value was adjusted to 7.0 using 0.1 M NaOH solution. Then, the collagen solution was evenly dropped on MS, and the collagen solution was allowed to self-assemble at 37 °C for 1 h to form MS@Col. Additionally, 10 mL of CMC solution and 1 mL of GP solution were mixed and dropped onto MS@Col, and the fiber was assembled overnight at 37 °C to obtain MS@CMC-Col.

Characterization of Different Electrospun Fibers: SEM: The different electrospun fibers were cut to a suitable size and fixed on the SEM sample-making copper plate with a conductive adhesive. Then, they were put into the SEM (Hitachi, Japan) chamber after the surface was gold sprayed by the ion sputtering (Quorum, UK). The acceleration voltage was set to 10 kV to acquire the images, from which 100 fibers were randomly selected for diameter analysis using ImageJ.

Particle Size Analysis: The size of HA particles in the micro-sol was measured using a DLS particle size analyzer (Malvern, UK).

TEM and Cytokine Distribution: The electrospun fibers were collected randomly and rapidly during the electrospinning process using a duplex copper mesh (Zhongjing Koyi, Henan, China), and the internal structure of single fibers was observed using TEM (FEI, USA) system operating at 120 kV. The fluorescent electrospinning solution was prepared using fluorescein isothiocyanate (FITC) labeled BSA (Solarbio, Beijing, China) instead of IL-4 wrapped in the micro-sol, followed by electrospinning with light avoidance. Fluorescent electrospun fibers were collected with a carrier slice and photographed using fluorescence microscopy.

EDS: To compare the changes in chemical elements on the surfaces of different fiber membranes, different electrospun fibers were analyzed using EDS (FEI, USA).

FTIR: FTIR (Thermo Scientific, USA) was used to analyze the chemical compositions of different electrospun fibers.

Water Contact Angles: The water contact angles of different electrospun fibers were measured using a water contact angle analyzer (WCA, Germany) to assess the change in hydrophilicity/hydrophobicity.

Mechanical Testing: Electrospun fibers were cut into rectangular samples (15 × 3 × 0.1 mm), and the samples were set on a mechanical stretching apparatus (Hengyi, Shanghai, China). Data were collected at a mechanical sensor of 50 N and a speed of 10 mm min^{-1}, and the stress–strain curves were plotted using the obtained data.

Swelling Ratio: Electrospun fibers with initial weight M1 were submerged in PBS at room temperature for 24 h. After wiping off the excess water from the surface with absorbent paper, the electrospun fibers were weighed, and the values were recorded as M2. The swelling ratio (SR) was calculated as SR = (M2 – M1)/M1.

Mass Loss Ratio: Electrospun fibers with initial weight M0 were submerged in PBS at room temperature and PBS was changed every day. After freeze-drying at fixed time points (1, 3, 5, 7, 10, and 14 d), the electrospun fibers were weighed, and the values were recorded as Ma. The mass loss (ML) ratio was calculated as ML = (M0 – Ma)/M0.

Cytokine Release: 50 mg of MS, MS@Col, MS@CMC, and MS@CMC-Col (theoretically containing 100 ng of IL-4) was immersed in 50 mL centrifuge tubes containing 10 mL of PBS solution with 1% BSA. All centrifuge tubes were placed in a shaker at the constant temperature of 37 °C, and the vibration frequency was set to 100 rpm. The released solution was collected at specific time points (0.5, 1, 2, 3, 5, 7, 10, and 14 d) and stored in the refrigerator at -80 °C. Additionally, 10 mL of fresh PBS was added into the centrifuge tubes. The amount of IL-4 in the released solution was measured using an ELISA kit (MULTI, Hangzhou, China), and the cumulative release profile was plotted.

In Vitro Experiments: Cell Culture: Round cell creepers with a diameter of 14 mm and a thickness of 100 um were glued to aluminum foils to collect the electrospun fibers. After electrospinning, the creepers were vacuum dried overnight and placed in 75% ethanol solution for 30 min to hydrate and sterilize. Then, creepers with electrospun fibers were rinsed three times with PBS to remove residual ethanol and placed in 24-well plates. Assembly of the hydrogel coating was carried out following the steps in 4.2. After soaking in 75% ethanol and UV irradiation overnight, the culture medium was added to 24-well plates for immersion.

Figure 10. IHC analysis of OCN, CD31, and periostin. A) Immunohistochemical staining of OCN at 4 and 8 weeks. B) Immunohistochemical staining of CD31 at 4 and 8 weeks. C) Immunohistochemical staining of periostin at 4 and 8 weeks. D,E) Immunohistochemical optical density of OCN at 4 and 8 weeks. F,G) Immunohistochemical optical density of CD31 at 4 and 8 weeks. H, I) Immunohistochemical optical density of periostin at 4 and 8 weeks. (Statistical analysis entails one-way ANOVA followed by Tukey's multiple comparison test; $n = 5$; ns, not statistically significant; $^{*}p < 0.05$; $^{**}p < 0.01$; $^{***}p < 0.001$.)

Primary rat BMSCs were obtained from rat femurs and tibias after isolation and culture. Rat Mφ were purchased from Wuhan Procell Life Science and Technology Co. After the cells were digested in the culture dishes, they were counted three times under the light microscope to obtain the average cell concentration. Then, the cells were inoculated on different electrospun fibers with the number of cells corresponding to different experiments. With the appropriate medium added, the cells were placed in the cell culture chamber for culture. The medium was changed every 2 to 3 d. The cell culture chamber was set to 37 °C, 95% relative humidity, and 5% CO_2.

Cell Proliferation: In total, 1×10^4 BMSCs were grown in 24-well plates containing different electrospun fibers as described above, and cell creepers without electrospun fibers were set as the control group. The medium was replaced with the mixture of 100 µL CCK8 reagent (Dojindo, Japan) and 900 µL medium on days 1, 3, 5, and 7 of culture. After 4 h of incubation in the cell culture incubator, 100 µL of the mixture was transported into 96-well plates. Then, the absorbance at a wavelength of 450 nm was measured using a microplate reader.

Live/Dead Staining: BMSCs were incubated with different electrospun fibers for 3 d. Then, the medium was removed, and the cells were washed three times with prewarmed (37 °C) PBS. A working solution of Live/Dead staining was configured following the instructions, specifically 300 µL of the working solution of Live/Dead staining was added to each well and incubated for 30 min at room temperature in the dark. After removing the working solution, the cells were observed under an inverted fluorescence microscope. Live cells were labeled with green fluorescence, while dead cells were labeled with red fluorescence.

Mechanism of Cell Adhesion: BMSCs were co-cultured on different electrospun fibers for 24 h, and immunofluorescence staining was performed using integrin β1 primary antibody (Novus, USA) and vinculin primary antibody (Novus, USA). Briefly, the medium in each well was removed, and the cells were fixed with 4% paraformaldehyde for 30 min. After rinsing three times with PBS, the cells were treated with 0.3% Triton for 30 min. After rinsing three times, the cells were closed with rapid closure solution (Beyotime, China) for 1 h. After rinsing three times, the corresponding primary antibodies were added and incubated overnight at 4 °C. The next day, the secondary antibody (Abcam, USA) was added after three rinses and incubated at 37 °C for 2 h. The secondary antibody was washed off, the cytoskeleton was incubated with phalloidin (Yearsen, China) at room temperature for 30 min, and the nucleus was stained with DAPI (Yearsen, China) for 5 min. The immunofluorescent cells were observed and photographed using an inverted fluorescence microscope.

Cell Chemotactic Migration Assay: BMSCs (1×10^4) suspended in 150 µL of basic medium were added to the upper chamber of a 24-well transwell plate (pore size of 8 mm, Corning, USA). After coculture fibrous membrane and Mφ for 3 d, 700 µL of the supernatant of the cell culture medium was collected and added to the lower chamber. After 24 h of coculture, the upper surface of the polycarbonate membrane was gently wiped with a cotton swab to remove the adherent cells. Cells migrated to the lower surface were then fixed with 4% paraformaldehyde for 30 min, and stained with 1% crystal violet solution (Beyotime, China) for 30 min after rinsing three times. After drying, the membrane was examined and photographed under the light microscope. The number of cells obtained from five views was randomly recorded under the microscope for comparison among the groups.

Mφ Phenotype Analysis: Mφ was cocultured with different electrospun fibers at a density of 5×10^4 mL^{-1}. Subsequently, cells were labeled with F4/80 (Abcam, USA), INOS (Abcam, USA), and CD206 (Abcam, USA) primary antibodies on days 3 and 7 of culture. Then, cells were fixed with 4% paraformaldehyde, closed with rapid closure solution, and incubated with primary/secondary antibodies and DAPI, in order, as described above. Immunofluorescent cells were observed and photographed under an inverted fluorescence microscope.

Mφ were cocultured with different electrospun fibers. After 3 and 7 d of culture, the cells were collected and examined using a flow cytometer (BD, Canto II, USA). We checked to ensure that the remaining cells on the scaffold were less than 20% in five random fields of vision after collecting the cells. Briefly, the collected cells were transferred to 1.5 mL Eppendorf (EP) tubes and centrifuged at 2000 rpm for 5 min at 4 °C, followed by sequential addition of anti-CD45-FITC (BD Pharmingen, USA), anti-CD11b-PEcy7 (BD Pharmingen, USA), anti-CD86-APC (BD Pharmingen, USA), anti-CD86-APC (BD Pharmingen, USA), and anti-CD206-PE (BD Pharmingen, USA). The labeled cells were incubated at 4 °C for 30 min. The number of cells in each group of scaffolds was more than 1×10^4 when tested by flow cytometry. The cells were analyzed with FlowJo. For analysis, cells were first circled by CD45 and CD11b, followed by CD86 and CD206 in sequence.

Detection of Mφ Secretory Factors: Mφ were cocultured with different electrospun fibers, and the supernatants of the cell culture medium were collected. The contents of TNF-α, IL10, VEGF, PDGF-BB, TGF-β1, and BMP-2 in the supernatants were quantified by the corresponding ELISA kits (Elabscience, Wuhan, China) per instructions.

Quantitative Real Time Polymerase Chain Reaction (qRT-PCR) of Mφ-Related Genes: Mφ were collected after 3 and 7 d of coculture with different electrospun fibers. The genes of TNF-α, IL10, INOS, and Arg-1 were detected using qRT-PCR. Briefly, total RNAs were extracted using TRIzol reagent (Invitrogen, USA), followed by reverse transcription of RNAs using Takara reverse transcription kit (Takara, Japan) following the operating instructions. qRT-PCR was conducted using Takara polymerase chain reaction kit (Takara, Japan). GAPDH was used as the internal reference. The primer sequences were designed by PubMed and synthesized by Shanghai Generay (Table S1, Supporting Information).

WB: Mφ were collected after 7 d of coculture with different electrospun fibers, and the expressions of related proteins were examined using WB. Briefly, total protein was extracted using RIPA lysis buffer (Beyotime, Shanghai, China), and protein lysis products were quantified using a bicinchoninic acid (BCA) kit (Solarbio, Beijing, China). Subsequently, 20 µg of protein was loaded onto 10% SDS PAGE gels (New Cell & Molecular, Suzhou, China), followed by electrophoresis, membrane transfer, and closure. Then, the membranes were incubated with primary antibodies of p-STAT6 (CST, USA), STST6 (CST, USA), p-PI3K (CST, USA), PI3K (CST, USA), p-AKT (CST, USA), AKT (CST, USA), p-NF-κb (CST, USA), NF-κb (CST, USA), and GAPDH (CST, USA). The membranes were incubated with the secondary antibody solution labeled by horseradish peroxidase (HRP) (Beyotime, Shanghai, China), and the protein bands were detected using enhanced chemiluminescence (ECL) kit (Thermo Fisher, USA) and scanned by gel imaging system.

Angiogenesis Experiment of HUVECs: First, Mφ were cocultured with different electrospun fibers for 7 d, and then the supernatant of the cell culture medium was collected and mixed with unused culture medium at a ratio of 1:1 to prepare HUVECs-specific medium. Before the angiogenesis experiment, 200 µL of low growth factor matrix gel (Corning, USA) was added to 24-well plates and placed in the cell culture incubator for 1 h. HUVECs were inoculated in 24-well plates coated with low growth factor matrix gel at a density of 1×10^5 mL^{-1}, and the HUVECs-specific medium was added. After incubation for 3 and 6 h, the cells were fixed with 4% paraformaldehyde. Then, the cytoskeleton and nucleus of HUVECs were stained as described above. The stained cells were observed and photographed under an inverted fluorescence microscope.

Osteogenic Differentiation: Mφ and BMSCs were cocultured using 24-well transwell cell culture plates (Corning, USA). Mφ were cultured on electrospun fibers in the upper chamber, while BMSCs were cultured on electrospun fibers in the lower chamber. After 7 d of co-culture, BMSCs of different groups were stained and quantified using the ALP chromogenic solution kit (Beyotime, Shanghai, China) and the alkaline phosphatase activity quantification kit (Jiancheng, Nanjing, China). After 14 d of coculture, immunofluorescence staining of BMSCs in different groups was performed using OCN primary antibody (SAB, USA) following the immunofluorescence staining procedure described above. After 21 d of coculture, BMSCs were stained using a cytosine red calcium staining kit (Cyagen, Guangzhou, China). The calcium nodules were detected by light microscopy and photographed. Then, the calcium nodules were lysed using perchloric acid to measure the absorbance at a wavelength of 420 nm using a microplate reader.

qRT-PCR for Osteogenesis-Related Genes: BMSCs, cultured for 7 d as described, were collected. The gene expressions of ALPL and RUNX-2 were detected using the qRT-PCR method described above. BMSCs cultured for 14 d were collected. The gene expressions of OCN and OPN were detected using the qRT-PCR method. GAPDH was used as the internal reference gene.

In Vivo Experiments: Preparation of Experimental Animals: All Sprague Dawley (SD) rats were purchased from Zhaoyan (Suzhou) New Drug Research Center Co., Ltd. All rats were male with an average weight of 200–220 g. All animal handling and surgical operations during the experiments were approved by the Ethics Committee of the First Affiliated Hospital of Soochow University.

Construction of Rat Cranial Defect Models and Implantation of Bionic Periosteum: Briefly, SD rats were first anesthetized with 2% pentobarbital at a dose of 2.5 mL kg^{-1}. After complete anesthesia, the skull of the rats was shaved and prepared for skin disinfection with anion. A median incision of approximately 2.5 cm in length was made along the longitudinal axis of the skull. The skin and fascia were separated layer by layer until the skull was exposed. Two round defects were made on both sides of the skull with a dental ring drill with a diameter of 5 mm. After rinsing and hemostasis, the bone defect area was covered with different sterilized electrospun fibers, and the one without any materials was set as the control group. Then, the incision was sutured layer by layer and disinfected with iodophor. Penicillin was injected intramuscularly for 3 d from the day of surgery to prevent infection.

Acquisition of Animal Specimens: SD rats were euthanized at 3 days, 7 days, 4 weeks, and 8 weeks after surgery. The cranial specimens from different groups were collected and fixed in 10% formalin for 24 h. Specimens from 3 and 7 d after surgery were used for the analysis of Mφ polarization and secretion of related inflammatory factors, and specimens from 4 and 8 weeks after surgery were used to evaluate bone defect repair.

Micro-CT Analysis: Cranial bone samples from 4 and 8 weeks after surgery were scanned and processed using micro-CT (SkyScan, SkyScan 1176 Belgium). The scanning voltage was 65 kV, current was 385 mA, and resolution was 7 µm. The scanned data were analyzed with the corresponding software to obtain BV/TV, BMD, and BS repair ratios. The scanned cranial bone samples were also reconstructed on the surface using the Mimic software.

Histological Analysis: The collected cranial bone samples were fixed in 10% formalin for 24 h and then decalcified using ethylene diamine tetra acetic acid (EDTA) solution for 2 weeks, followed by gradient dehydration with different concentrations of ethanol solution. Dehydrated samples were soaked in pure xylene solution and then embedded in paraffin. Histological analysis was divided into two parts. Specimens from 3 and 7 d after surgery were decalcified, embedded, and sectioned as described above. The samples were labeled with antibodies of INOS (Servicebio, China), Arg-1 (Servicebio, China), TNF-α (Servicebio, China), and IL-10 (Servicebio, China) for immunofluorescence staining to detect the phenotype changes of Mφ and related inflammatory parameters in vivo. Specimens from 4 and 8 weeks after surgery were treated with hematoxylin and eosin (H&E) staining and Masson staining to analyze bone regeneration, followed by immunohistochemical staining for OCN (Servicebio, China), periostin (Abcam, China) and CD31 (Servicebio, China) to assess the bone tissue, periosteum regeneration, and vascularization of bone defects, respectively.

Statistical Analysis: All experimental data, expressed as mean ± standard deviation, were statistically analyzed and plotted using Graph Prism software or Origin software. The differences between groups were tested by one-way or multi-way ANOVA and Tukey's multiple comparison methods. Differences with statistical significance are marked by * $p < 0.05$, ** $p < 0.01$, *** $p < 0.001$, ****$p < 0.0001$, and differences with no statistical significance are marked by ns.

Supporting Information

Supporting Information is available from the Wiley Online Library or from the author.

Acknowledgements

Z.X., L.W., and Y.T. contributed equally to this work. This work was supported by the National Natural Science Foundation of China (81972078, 82120108017, 82102589, 81702190), Social Development Project of Jiangsu Province (BE2021646), Standardized Diagnosis and Treatment Project of Key Diseases in Jiangsu Province (BE2015641), the Natural Science Foundation of Jiangsu Province (BK20211504 and BK20170370), Jiangsu Innovative and Enterpreneurial Talent Programme (JSSCBS20211570), and Suzhou Gusu Health Talent Program (GSWS2020001 and GSWS2021007).

Conflict of Interest

The authors declare no conflict of interest.

Data Availability Statement

Research data are not shared.

Keywords

bionic periosteum, bone immune microenvironment, bone regeneration, macrophages, vascularization

Received: July 7, 2022
Revised: September 24, 2022
Published online: October 14, 2022

[1] a) K. Dai, S. Deng, Y. Yu, F. Zhu, J. Wang, C. Liu, *Bone Res.* **2022**, *10*, 1; b) A. Ho-Shui-Ling, J. Bolander, L. E. Rustom, A. W. Johnson, F. P. Luyten, C. Picart, *Biomaterials* **2018**, *180*, 143; c) N. Li, J. Song, G. Zhu, X. Li, L. Liu, X. Shi, Y. Wang, *Biomater. Sci.* **2016**, *4*, 1554.

[2] a) L. Liu, Y. Shang, C. Li, Y. Jiao, Y. Qiu, C. Wang, Y. Wu, Q. Zhang, F. Wang, Z. Yang, L. Wang, *Adv. Healthcare Mater.* **2021**, *10*, 2101195; b) X. Zhang, H. A. Awad, R. J. O'Keefe, R. E. Guldberg, E. M. Schwarz, *Clin. Orthop. Relat. Res.* **2008**, *466*, 1777; c) Q.-Q. Wan, K. Jiao, Y.-X. Ma, B. Gao, Z. Mu, Y.-R. Wang, Y.-H. Wang, L. Duan, K.-H. Xu, J.-T. Gu, J.-F. Yan, J. Li, M.-J. Shen, F. R. Tay, L.-N. Niu, *ACS Appl. Mater. Interfaces* **2022**, *14*, 14103.

[3] Z. Jamalpoor, A. Asgari, M. H. Lashkari, A. Mirshafiey, M. Mohsenzadegan, *Iran. J Allergy, Asthma Immunol.* **2018**, *17*, 398.

[4] a) L. Wu, Y. Gu, L. Liu, J. Tang, J. Mao, K. Xi, Z. Jiang, Y. Zhou, Y. Xu, L. Deng, L. Chen, W. Cui, *Biomaterials* **2020**, *227*, 119555; b) G. Yang, H. Liu, Y. Cui, J. Li, X. Zhou, N. Wang, F. Wu, Y. Li, Y. Liu, X. Jiang, S. Zhang, *Biomaterials* **2021**, *268*, 120561; c) X. Shi, L. Li, S. Ostrovidov, Y. Shu, A. Khademhosseini, H. Wu, *ACS Appl. Mater. Interfaces* **2014**, *6*, 11915; d) Y. Kang, L. Ren, Y. Yang, *ACS Appl. Mater. Interfaces* **2014**, *6*, 9622; e) W. Zhang, X. Wang, R. Zhang, R. He, T. Lei, R. D. K. Misra, H. Nie, C. Ma, N. Lin, Z. Wang, *Colloids Surf., B* **2022**, *214*, 112459.

[5] a) F. Loi, L. A. Cordova, J. Pajarinen, T. H. Lin, Z. Yao, S. B. Goodman, *Bone* **2016**, *86*, 119; b) N. Yang, Y. Liu, *Int. J. Med. Sci.* **2021**, *18*, 3697.

[6] a) J. Pajarinen, T. Lin, E. Gibon, Y. Kohno, M. Maruyama, K. Nathan, L. Lu, Z. Yao, S. B. Goodman, *Biomaterials* **2019**, *196*, 80; b) J. Lee, H. Byun, S. K. Madhurakkat Perikamana, S. Lee, H. Shin, *Adv. Healthcare Mater.* **2019**, *8*, 1800861; c) Y.-H. Kim, R. O. C. Oreffo, J. I. Dawson, *Bone* **2022**, *159*, 116389.

[7] a) P. Guihard, Y. Danger, B. Brounais, E. David, R. Brion, J. Delecrin, C. D. Richards, S. Chevalier, F. Redini, D. Heymann, H. Gascan, F. Blanchard, *Stem Cells* **2012**, *30*, 762; b) K. L. Spiller, R. R. Anfang, K. J. Spiller, J. Ng, K. R. Nakazawa, J. W. Daulton, G. Vunjak-Novakovic, *Biomaterials* **2014**, *35*, 4477.

[8] a) Y. Zhang, T. Böse, R. E. Unger, J. A. Jansen, C. J. Kirkpatrick, J. J. J. P. van den Beucken, *Cell Tissue Res.* **2017**, *369*, 273; b) J. Muñoz, N. S. Akhavan, A. P. Mullins, B. H. Arjmandi, *Nutrients* **2020**, *12*, 2999.
[9] a) R. A. Bank, J. Zandstra, H. Room, A. H. Petersen, S. M. van Putten, *Tissue Eng., Part A* **2017**, *23*, 1078; b) Z. Chen, T. Klein, R. Z. Murray, R. Crawford, J. Chang, C. Wu, Y. Xiao, *Mater. Today* **2016**, *19*, 304.
[10] a) C. Schlundt, H. Fischer, C. H. Bucher, C. Rendenbach, G. N. Duda, K. Schmidt-Bleek, *Acta Biomater.* **2021**, *133*, 46; b) J. R. Alhamdi, T. Peng, I. M. Al-Naggar, K. L. Hawley, K. L. Spiller, L. T. Kuhn, *Biomaterials* **2019**, *196*, 90; c) W. Qiao, H. Xie, J. Fang, J. Shen, W. Li, D. Shen, J. Wu, S. Wu, X. Liu, Y. Zheng, K. M. C. Cheung, K. W. K. Yeung, *Biomaterials* **2021**, *276*, 121038.
[11] Z. W. Zheng, Y. H. Chen, D. Y. Wu, J. B. Wang, M. M. Lv, X. S. Wang, J. Sun, Z. Y. Zhang, *Theranostics* **2018**, *8*, 5482.
[12] a) E. M. O'Brien, G. E. Risser, K. L. Spiller, *Adv. Drug Delivery Rev.* **2019**, *149-150*, 85; b) L. Batoon, S. M. Millard, L. J. Raggatt, A. R. Pettit, *Curr. Osteoporosis Rep.* **2017**, *15*, 385.
[13] a) R. L. Gieseck 3rd, M. S. Wilson, T. A. Wynn, *Nat. Rev. Immunol.* **2018**, *18*, 62; b) M. F. Linton, J. J. Moslehi, V. R. Babaev, *Int. J. Mol. Sci.* **2019**, *20*, 2703; c) C. D. Mills, K. Ley, *J. Innate Immun.* **2014**, *6*, 716.
[14] a) S. Chen, W. Yao, H. Wang, T. Wang, X. Xiao, G. Sun, J. Yang, Y. Guan, Z. Zhang, Z. Xia, M. Li, Y. Tao, Z. Hei, *Theranostics* **2022**, *12*, 4904; b) P. Zare, M. Pezeshki-Modaress, S. M. Davachi, P. Zare, F. Yazdian, S. Simorgh, H. Ghanbari, H. Rashedi, Z. Bagher, *Carbohydr. Polym.* **2021**, *266*, 118123; c) N. Zhang, J. Lin, V. P. H. Lin, U. Milbreta, J. S. Chin, E. G. Y. Chew, M. M. Lian, J. N. Foo, K. Zhang, W. Wu, S. Y. Chew, *Adv. Sci.* **2021**, *8*, 2100805; d) B. Maharjan, J. Park, V. K. Kaliannagounder, G. P. Awasthi, M. K. Joshi, C. H. Park, C. S. Kim, *Carbohydr. Polym.* **2021**, *251*, 117023.
[15] a) J. Li, D. J. Mooney, *Nat. Rev. Mater.* **2016**, *1*, 16071; b) L. Elviri, A. Bianchera, C. Bergonzi, R. Bettini, *Expert Opin. Drug Delivery* **2017**, *14*, 897; c) X. Wang, O. Ronsin, B. Gravez, N. Farman, T. Baumberger, F. Jaisser, T. Coradin, C. Helary, *Adv. Sci.* **2021**, *8*, 2004213.
[16] C. Zhao, P. Qiu, M. Li, K. Liang, Z. Tang, P. Chen, J. Zhang, S. Fan, X. Lin, *Mater. Today Bio* **2021**, *12*, 100142.
[17] a) W. Ma, M. Zhou, W. Dong, S. Zhao, Y. Wang, J. Yao, Z. Liu, H. Han, D. Sun, M. Zhang, *J. Mater. Chem. B* **2021**, *9*, 7492; b) W. Zhang, N. Wang, M. Yang, T. Sun, J. Zhang, Y. Zhao, N. Huo, Z. Li, *J. Orthop. Transl.* **2022**, *33*, 41.
[18] S. C. Neves, L. Moroni, C. C. Barrias, P. L. Granja, *Trends Biotechnol.* **2020**, *38*, 292.
[19] T. Liu, W. Liu, L. Zeng, Z. Wen, Z. Xiong, Z. Liao, Y. Hu, *ACS Appl. Mater. Interfaces* **2022**, *14*, 41764.
[20] X. Zhao, L. Zhou, Q. Li, Q. Zou, C. Du, *Carbohydr. Polym.* **2018**, *195*, 225.
[21] a) L. Zhao, W. Lan, X. Dong, H. Xu, L. Wang, Y. Wei, J. Hou, D. Huang, W. Chen, *J. Biomater. Sci., Polym. Ed.* **2021**, *32*, 2195; b) B. M. Oosterlaken, M. P. Vena, G. de With, *Adv. Mater.* **2021**, *33*, 2004418; c) R. Budiraharjo, K. G. Neoh, E. T. Kang, A. Kishen, *Int. Endod. J.* **2010**, *43*, 930; d) X. Jing, B. Xie, X. Li, Y. Dai, L. Nie, C. Li, *Dent. Mater.* **2021**, *37*, 19; e) L. Upadhyaya, J. Singh, V. Agarwal, R. P. Tewari, *J. Controlled Release* **2014**, *186*, 54; f) L. Yu, K. Xia, C. Gong, J. Chen, W. Li, Y. Zhao, W. Guo, H. Dai, *Int. J. Biol. Macromol.* **2020**, *160*, 101.
[22] J. Shao, L. Weng, J. Li, H. Lin, H. Wang, J. Lin, *ACS Biomater. Sci. Eng.* **2022**, *8*, 610.
[23] a) Y. Yu, S. Xu, S. Li, H. Pan, *Biomater. Sci.* **2021**, *9*, 1583; b) C. Shortridge, E. Akbari Fakhrabadi, L. M. Wuescher, R. G. Worth, M. W. Liberatore, E. Yildirim-Ayan, *Int. J. Mol. Sci.* **2021**, *22*, 1134;
[24] Y. Xu, W. Cui, Y. Zhang, P. Zhou, Y. Gu, X. Shen, B. Li, L. Chen, *Adv. Healthcare Mater.* **2017**, *6*, 1601457.
[25] M. F. Butler, Y.-F. Ng, P. D. A. Pudney, *J. Polym. Sci., Part A: Polym. Chem.* **2003**, *41*, 3941.
[26] M. Jurak, A. E. Wiacek, A. Ladniak, K. Przykaza, K. Szafran, *Adv. Colloid Interface Sci.* **2021**, *294*, 102451.
[27] Q. Zhou, J. Lyu, G. Wang, M. Robertson, Z. Qiang, B. Sun, C. Ye, M. Zhu, *Adv. Funct. Mater.* **2021**, *31*, 25.
[28] P. Moreno-Layseca, J. Icha, H. Hamidi, J. Ivaska, *Nat. Cell Biol.* **2019**, *21*, 122.
[29] M. Hakariya, Y. Arisaka, H. Masuda, T. Yoda, A. Tamura, T. Iwata, N. Yui, *Gels* **2021**, *7*, 168.
[30] J. L. Bays, K. A. DeMali, *Cell. Mol. Life Sci.* **2017**, *74*, 2999.
[31] K. Xi, Y. Gu, J. Tang, H. Chen, Y. Xu, L. Wu, F. Cai, L. Deng, H. Yang, Q. Shi, W. Cui, L. Chen, *Nat. Commun.* **2020**, *11*, 4504.
[32] B. H. Cha, S. R. Shin, J. Leijten, Y. C. Li, S. Singh, J. C. Liu, N. Annabi, R. Abdi, M. R. Dokmeci, N. E. Vrana, A. M. Ghaemmaghami, A. Khademhosseini, *Adv. Healthcare Mater.* **2017**, *6*, 1700289.
[33] a) J.-Y. Bai, Y. Li, G.-H. Xue, K.-R. Li, Y.-F. Zheng, Z.-Q. Zhang, Q. Jiang, Y.-Y. Liu, X.-Z. Zhou, C. Cao, *Theranostics* **2021**, *11*, 4894; b) G. Ge, J. Bai, Q. Wang, X. Liang, H. Tao, H. Chen, M. Wei, J. Niu, H. Yang, Y. Xu, Y. Hao, Y. Xue, D. Geng, *Sci. China: Life Sci.* **2022**, *65*, 588.
[34] a) L. Chen, C. Yu, Y. Xiong, K. Chen, P. Liu, A. C. Panayi, X. Xiao, Q. Feng, B. Mi, G. Liu, *Bioact Mater* **2022**, https://doi.org/10.1016/j.bioactmat.2022.07.030; b) N. Su, C. Villicana, F. Yang, *Biomaterials* **2022**, *286*, 121604.
[35] C. Yang, Y. Yu, X. Wang, Q. Wang, L. Shang, *Eng. Regener.* **2021**, *2*, 171.
[36] S. C. Manolagas, *PLoS Genet.* **2020**, *16*, e1008714.
[37] T. Anada, C. C. Pan, A. M. Stahl, S. Mori, J. Fukuda, O. Suzuki, Y. Yang, *Int. J. Mol. Sci.* **2019**, *20*, 1096.
[38] R. Fu, W. C. Lv, Y. Xu, M. Y. Gong, X. J. Chen, N. Jiang, Y. Xu, Q. Q. Yao, L. Di, T. Lu, L. M. Wang, R. Mo, Z. Q. Wu, *Nat. Commun.* **2020**, *11*, 460.
[39] J. Li, W. Hou, Y. Yang, Q. Deng, H. Fu, Y. Yin, K. Duan, B. Feng, T. Guo, J. Weng, *Colloids Surf., B* **2022**, *218*, 112700.
[40] A. Kudo, *Adv. Exp. Med. Biol.* **2019**, *1132*, 43.